Article

Current Biology

Selection-driven color variation in the aposematic strawberry poison frog, *Oophaga pumilio*

Graphical abstract

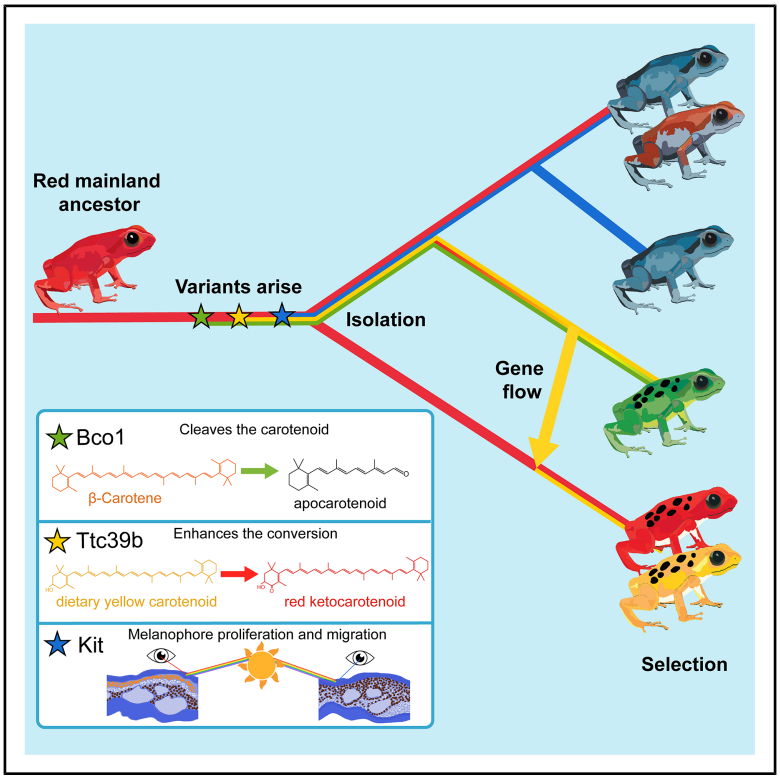

Authors

Diana Aguilar-Gómez, Layla Freeborn, Lin Yuan, ..., Kevin J. McGraw, Corinne L. Richards-Zawacki, Rasmus Nielsen

Correspondence

dianaguilr@gmail.com (D.A.-G.), cori.zawacki@pitt.edu (C.L.R.-Z.), rasmus_nielsen@berkeley.edu (R.N.)

In brief

Aguilar-Gómez et al. use exome sequencing of 347 strawberry poison frogs to uncover the genetic basis of color variation. They identify that *kit*, *ttc39b*, and *bco1* underlie blue-red, yellow-red, and green variation, respectively, and show that repeated selection on standing variation drives diversification of warning coloration.

Highlights

- Exome sequencing reveals the genetic basis of color variation in *Oophaga pumilio*
- *kit*, *ttc39b*, and *bco1* underlie blue-red, yellow-red, and green variation
- Color haplotypes predate population divergence and show selective sweep signals
- Recurrent selection on standing variation drives repeated warning color evolution

Aguilar-Gómez et al., 2026, Current Biology *36*, 1–18
March 23, 2026
https://doi.org/10.1016/j.cub.2026.01.041

CellPress

Please cite this article in press as: Aguilar-Gómez et al., Selection-driven color variation in the aposematic strawberry poison frog, *Oophaga pumilio*, Current Biology (2026), https://doi.org/10.1016/j.cub.2026.01.041

Current Biology

CellPress
OPEN ACCESS

Article

Selection-driven color variation in the aposematic strawberry poison frog, *Oophaga pumilio*

Diana Aguilar-Gómez,[1,2,13,*] Layla Freeborn,[3,4] Lin Yuan,[5] Lydia L. Smith,[6] Alex Guzman,[1,6] Andrew H. Vaughn,[1] Emma Steigerwald,[6] Adam Stuckert,[7] Yusan Yang,[3,8] Tyler Linderoth,[6,9] Matthew MacManes,[10] Kevin J. McGraw,[11] Corinne L. Richards-Zawacki,[3,12,*] and Rasmus Nielsen[1,6,*]

[1]Center for Computational Biology, University of California, Berkeley, Berkeley, CA 94720, USA
[2]Department of Ecology and Evolutionary Biology, University of California, Los Angeles, Los Angeles, CA 90095, USA
[3]Department of Biological Sciences, University of Pittsburgh, Pittsburgh, PA 15260, USA
[4]Research Computing, Office of Information Technology, University of Colorado, Boulder, Boulder, CO 80309, USA
[5]School of Life Sciences, The Chinese University of Hong Kong, Hong Kong, Hong Kong SAR, China
[6]Museum of Vertebrate Zoology, University of California, Berkeley, Berkeley, CA 94720, USA
[7]Department of Biology and Biochemistry, University of Houston, Houston, TX 77204, USA
[8]Department of Integrative Biology, University of South Florida, Tampa, FL 33620, USA
[9]W.K. Kellogg Biological Station, Michigan State University, MI 49060, USA
[10]Department of Molecular, Cellular and Biomedical Sciences, University of New Hampshire, Durham, NH 03824, USA
[11]Department of Integrative Biology, Michigan State University, East Lansing, MI 48824, USA
[12]Smithsonian Tropical Research Institute, Panama City 0843-03092, Panama
[13]Lead contact
*Correspondence: dianaguilr@gmail.com (D.A.-G.), cori.zawacki@pitt.edu (C.L.R.-Z.), rasmus_nielsen@berkeley.edu (R.N.)
https://doi.org/10.1016/j.cub.2026.01.041

SUMMARY

The strawberry poison frog, *Oophaga pumilio*, is a striking example of natural color variation, making it a valuable system for studying the genetic and evolutionary mechanisms underlying phenotypic diversity. While most populations of this poisonous frog are bright red, frogs from Bocas del Toro Province, Panama, exhibit remarkable variation in color, both within and among island populations. This diversity in warning coloration challenges conventional models of aposematism and has fueled extensive debate about its evolutionary and genetic origins. A major obstacle to understanding this phenomenon has been the species' large genome (~6.7 Gb). To address this, we sequenced exomes from 347 individuals across ten populations and identified genetic factors associated with color variation. Our analyses identified *kit* as a major candidate gene linked to blue-red polymorphism, where an increase in the proportion and organization of melanosomes with respect to other pigments contributes to blue coloration. Variation in *ttc39b*, a gene involved in conversion from yellow to red carotenoids, is strongly associated with the yellow-red polymorphism. We also identify *bco1*, a carotenoid-cleaving gene, which shows strong evidence of population differentiation and higher expression in green frogs. The haplotypes at all three loci predate population divergence and exhibit signatures of selective sweeps, indicating that selection has repeatedly acted on standing genetic variation in different populations. Our findings support a dynamic evolutionary model in which new morphs emerge through a balance of selective pressures, including predation, intraspecific competition, and mate choice.

INTRODUCTION

The strawberry poison frog, *Oophaga pumilio*, has bright red coloration in most of its continental distribution in Central America.[1] This coloration functions in aposematism as a warning signal to predators.[2] However, in the Bocas del Toro Province of Panama, this species exhibits remarkable variation in color and pattern.[3] Colors on the islands include yellow, orange, red, green, blue, and some intermediate phenotypes (Figure 1A). The formation of the Bocas del Toro archipelago was recent—1,000–9,000 years ago[4]—suggesting that the dramatic phenotypic differences emerged in a very short period of time. Most color variation is found between islands (polytypism),[5] with each allopatric population being monomorphic. However, a few areas have sympatric variation (polymorphism).[6] This variation has made *O. pumilio* a model for understanding the mechanisms underlying the maintenance of phenotypic variation, with numerous studies on *O. pumilio* focused on its ecology,[3,7–11] toxicity,[1,12] sexual selection,[13–15] natural selection,[10,16] and population history.[17]

Standard theory on aposematism suggests that natural selection acts to reduce warning signal variation.[2,18] For example, if red coloration is recognized and avoided by predators, selection would act against new mutations that give rise to alternative colors, making the high degree of phenotypic variability observed in Bocas del Toro somewhat enigmatic. Several hypotheses have been proposed to explain the emergence and maintenance of this variation in *O. pumilio*. Some of them include (1) viability selection, where color variation may have evolved as

Please cite this article in press as: Aguilar-Gómez et al., Selection-driven color variation in the aposematic strawberry poison frog, *Oophaga pumilio*, Current Biology (2026), https://doi.org/10.1016/j.cub.2026.01.041

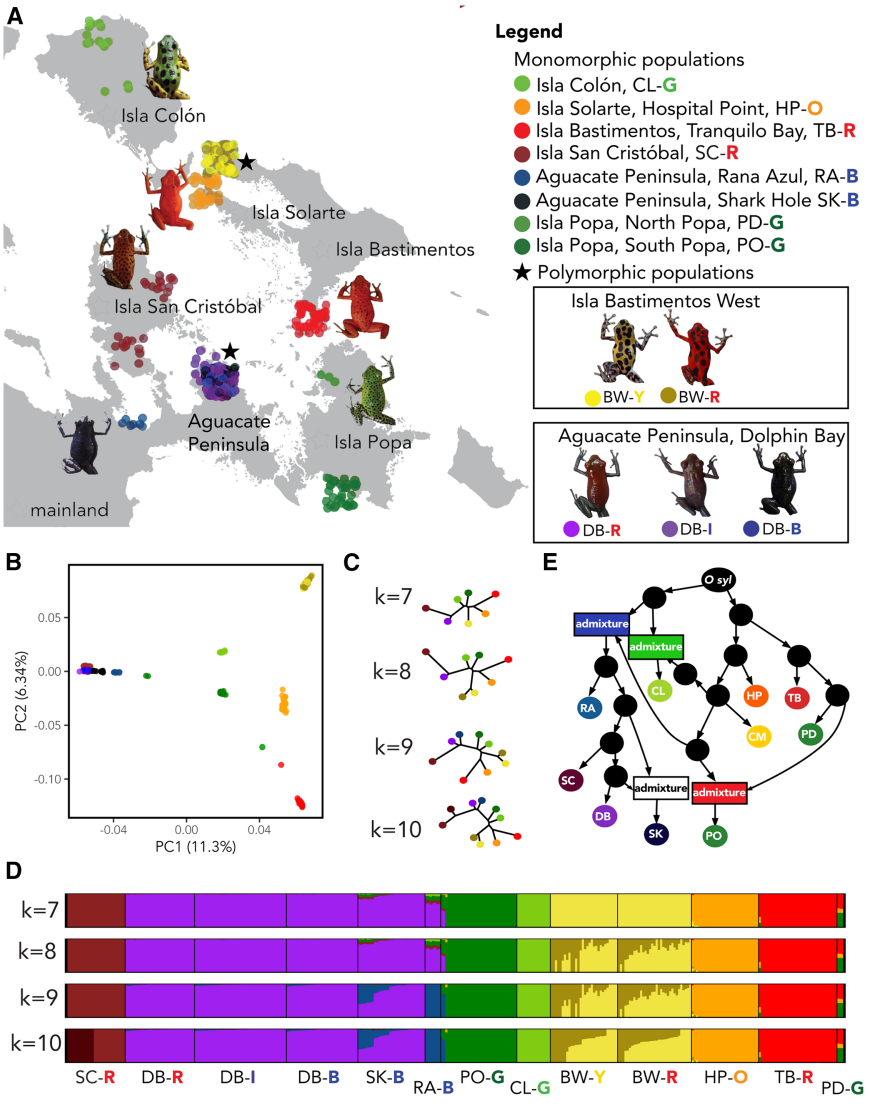

Figure 1. Population structure of *Oophaga pumilio* in Bocas del Toro archipelago

(A) Sampling locations, population labels, and colors used in PCA. Labels of populations have an added letter to specify the color of the individuals (R, red; I, intermediate; B, blue; G, green; Y, yellow; and O, orange).

(B) PCA of genome-wide variation.

(C) Trees of relationship between ancestry components using k = 7 to k = 10.

(D) Structure plot of how ancestry components are distributed in different populations, using the same colors as in (C).

(E) Topology using four migration/admixture events with the highest probability (45%).

See also Figure S1, Table S1, and Data S1.

an adaptation to different environments or predators as an honest signal of toxicity[7,12,19]; (2) geographic isolation, since most morphs are restricted to different islands[17,20]; (3) a lack of predators combined with neutral drift[21]; and (4) sexual selection, in the form of female mate choice and male-male competition.[6,14,22,23] Many of these hypotheses and mechanisms are not mutually exclusive, with most authors agreeing that several factors are likely responsible for this variation.[3,17,20,24] *Oophaga pumilio* has complex parental care, and tadpoles learn to recognize traits of their parents (i.e., imprinting), which may influence their own mating behavior later in life.[6] *Oophaga pumilio* shows evidence of assortative mate preferences, whereby females[25] prefer to mate with males of their own morph.[26,27] Additionally, males compete by defending territories and are generally more aggressive toward males of their own morph, leading to the possibility of sexual selection favoring rare morphs.[13,22] Imprinting, female bias, and male bias together are the main reasons why sexual selection is often suggested to drive the maintenance and divergence of these morphs.[6] However, a central question is whether neutral processes involving genetic drift, geographic isolation, and potential changes in predation pressure[28] can explain the observed phenotypic variation, or if selection has to be invoked. Furthermore, can selection drive the spread of new color variants locally despite the standard theory on aposematism asserting that selection should act against new variants?

Our aim in this project is to understand the genetic basis of color in *O. pumilio* and the evolutionary mechanisms that produce the array of variation in Bocas del Toro. Because coloration is ultimately a product of underlying cellular and molecular structures, understanding its proximate mechanisms is key to interpreting its evolutionary significance. In particular, by identifying genes, or genomic regions, that underlie phenotypic variation, we can determine if selection is acting on these regions and answer the question as to whether new color variants increase in frequency purely by genetic drift or if they are the target of selection and have increased in frequency because they confer a fitness advantage to the individuals carrying them.

In amphibians, color variation is primarily controlled by specialized pigment cells known as chromatophores, which are arranged in layers within the skin.[29–32] There are several types of chromatophores: melanophores (black/brown pigments), iridophores (structural reflectors), xanthophores (yellow/orange pigments), and erythrophores (red pigments).[29,30] The diversity of coloration and patterning arises from the relative abundance, spatial distribution, and interactions among these cell types, which are established during development.[33] In addition, some amphibians exhibit physiological color changes via contraction or expansion of these cells in response to environmental cues.[34]

In *O. pumilio*, the ancestral coloration is red,[35] but populations in Bocas del Toro exhibit orange, yellow, green, and blue morphs as well. Amphibians do not have chromatophores that produce

Please cite this article in press as: Aguilar-Gómez et al., Selection-driven color variation in the aposematic strawberry poison frog, *Oophaga pumilio*, Current Biology (2026), https://doi.org/10.1016/j.cub.2026.01.041

green or blue pigments. Instead, blue can be produced as a structural color from diffraction or interference of light[36] caused by specific layerings of different chromatophores, particularly iridophores beneath other pigment cells.[31,34] Green hues typically arise from the optical combination of this structural blue with yellow carotenoid pigments within xanthophores.[34] Since vertebrates cannot synthesize carotenoids *de novo*, they must obtain them from their diet, either depositing them directly or metabolizing them before incorporation into tissues.[32,37] As a result, frogs fed a diet richer in carotenoids can display brighter green coloration.[38,39] In some amphibians, green coloration may also result from *chlorosis*, the accumulation of the pigment biliverdin in bones or lymph, producing a blue-green tint.[40] However, dendrobatid frogs such as *O. pumilio* do not appear to have elevated biliverdin levels,[40,41] suggesting their blue/green coloration is largely a combination of structural and carotenoid mechanisms.

Previous genetic research on *O. pumilio* has been restricted to mitochondrial DNA, microsatellite,[42] amplified fragment length polymorphism (AFLP),[10] differential expression[43,44] studies, and RADSeq,[45] in addition to the generation of a reference genome.[46] However, population-scale genomic data for this species have been slow to come due to the large (~6.76 Gb) and highly repetitive genome, which makes this type of approach technically challenging and expensive. To address these challenges, we present exome sequencing data from 347 individuals from Bocas del Toro. We use genome-wide association studies (GWASs) coupled with selection scans to identify genes underlying the color polymorphisms and use further population genetic analyses of these genes to answer decades-old questions regarding the underlying genomic architecture of the Bocas del Toro skin color variation.

RESULTS

Population structure and demographic history in Bocas del Toro

To infer the population structure and history of the Bocas del Toro *O. pumilio*, we sampled 347 individuals from eight different morphs, each defined by a unique combination of skin patterning and coloration, denoted by locality abbreviation and color (B, blue; R, red; O, orange; G, green; Y, yellow; I, intermediate). Mainland populations from the Aguacate Peninsula include Rana Azul (RA-B), Shark Hole (SK-B), and Dolphin Bay (DB-B, DB-I, and DB-R). Island populations were sampled from Isla Bastimentos (Bastimentos West [BW-R and BW-Y] and Tranquilo Bay [TB-R]), Isla Solarte (Hospital Point [HP-O]), Isla Popa (North Popa [PD-G] and South Popa [PO-G]), Isla Colón (CL-G), and Isla San Cristóbal (SC-R) (Figure 1A). We performed principal-component analysis (PCA; Figure 1B) on 10,788,793 filtered SNPs. PC1 separates frogs geographically from east to west, except for the Popa morph, which is placed between TB-R and mainland morphs from the peninsula (SK, DB, and RA). PC2 correlates with a north-south axis of Isla Bastimentos (BW and TB). PC3 separates the SC-R morph from the mainland frogs from the peninsula (Figure S1).

We used the software suite OHANA[47] for unsupervised ancestry component assignment, testing different numbers of ancestral lineages, k, with k = 7 to k = 10. Most sampled populations are allocated to their own component using k = 7 (Figures 1C and 1D), except for the mainland morphs from the Aguacate Peninsula, which share a component. The Aguacate blue morph separates into RA-B and SK-B subpopulations at k = 9. Some SK-B frogs are admixed between DB and RA-B. Admixture analyses did not separate polymorphic populations BW (BW-Y and BW-R) and DB (DB-B and DB-R) into different ancestry components, even up to k = 10 components (Figures 1B and 1D). Three Popa morph individuals sampled in the north of Isla Popa (PD-G) are estimated to be admixed with the TB population and separate from other PO individuals in the PCA (Figure 1B).

We next calculated genome-wide pairwise F_{ST} (Table S1). Allopatric populations showed trends similar to previous studies using microsatellites and AFLPs.[10,17] Sympatric morphs within the same population (BW and DB) that could not be separated in the structure analysis or PCA have low values of F_{ST} (~0.01) and are indistinguishable based on a genome-wide neighbor-joining tree (Figure S1). Some populations within the same island are genetically differentiated. For example, TB and BW from Isla Bastimentos show no admixture and are more diverged genome-wide ($F_{ST} > 0.2$) than populations from different islands. By contrast, BW and the CL populations are on different islands and have lower divergence ($F_{ST} = 0.135$). Another example is that the PD population is slightly less diverged from the TB-R population on Bastimentos ($F_{ST} = 0.126$) than from the PO population ($F_{ST} = 0.133$). These comparisons illustrate that within-island divergence can approach or exceed among-island levels, even in phenotypically similar populations.

Previous studies detected no evidence of migration in Bocas del Toro.[17] However, using AdmixtureBayes,[48] we tested topologies with up to four admixture events (Figures 1E and S1). Topologies with fewer than four migration events were rejected by 4-population (ABBA/BABA) tests using *Oophaga sylvatica* as an outgroup (Data S1A–S1C), providing evidence for substantial migration among islands. For example, the topology recovered with 100% probability when specifying zero admixture events has the subgraph ([TB and PD] and PO; *O. sylvatica*), while the 4-population test shows ([PO and PD] TB; *O. sylvatica*) as the most prevalent topology. The top three topologies identified by AdmixtureBayes[48] represent 74% of the probability with four admixture events. Interpreting these topologies with respect to colonization scenarios suggests an ancestor from the mainland splitting into two lineages: one entering the archipelago from the north through CL and another from the south via the Aguacate Peninsula (Figures 1E and S1). The northern lineage subsequently splits into (HP and BW) and (TB and PD). The southern lineage is RA and SC (DB and SK), with admixture from RA to SK (as also seen in the OHANA analysis; Figure 1C). CL is admixed between north and south lineages, with its proximity to the mainland likely facilitating migration. Similarly, PO is admixed between PD and mainland ancestry. Isla Popa split from the Aguacate Peninsula ~1,000 years ago[4] and is currently separated by a small stretch of water (Figure S1). All three admixture topologies indicate bidirectional migration between the Aguacate Peninsula and Isla Popa. Our results suggest extensive gene flow between Bocas del Toro populations, contradicting a simple model of population splits without subsequent gene flow. Multiple colonization waves during past periods of lower sea level[4] and/or continued ongoing gene flow likely explain the observed patterns.

Please cite this article in press as: Aguilar-Gómez et al., Selection-driven color variation in the aposematic strawberry poison frog, *Oophaga pumilio*, Current Biology (2026), https://doi.org/10.1016/j.cub.2026.01.041

Table 1. Demographic model results

	Split with migration						
Pop1- Pop2	Nref	Nu1	Nu2	Split time years	Migration rate	LL	LLdata
BW-CL	6,548	21,779	12,699	44,070	5.09E−05	−126,920	−7,073
CL-HP	7,069	20,855	17,343	43,949	3.72E−05	−83,350	−3,774
CL-RA	6,901	21,774	14,560	39,208	4.51E−05	−29,900	−1,114
BW-SC	4,362	14,549	10,364	65,280	1.97E−05	−382,708	−11,173
DB-RA	9,130	20,381	12,403	29,304	2.24E−04	−49,822	−5,134
DB-SK	9,453	15,346	15,985	27,801	2.77E−03	−60,564	−8,849
DB-TB	6,251	20,280	16,896	58,762	2.08E−05	−630,758	−21,080
HP-PD	6,728	15,885	17,569	49,293	4.89E−05	−21,308	−1,049
HP-TB	2,922	15,331	14,953	77,852	4.45E−05	−209,593	−7,926
PD-TB	6,699	16,080	14,149	55,487	7.26E−05	−18,623	−1,201
PO-RA	6,711	20,674	13,415	41,544	5.68E−05	−35,125	−2,238
PO-SK	6,475	19,367	15,606	46,132	5.54E−05	−139,476	−7,458
SC-SK	6,793	7,714	18,835	46,689	8.00E−05	−137,605	−6,061
SC-TB	7,853	10,281	18,407	54,228	1.49E−05	−266,103	−6,850
BW-HP	4,047	11,974	16,922	65,906	4.89E−05	−304,227	−12,592

Pairwise demographic models with an ancestral population size, followed by split and migration. Models shown have the best log-likelihood per pair. Population abbreviations are the same as those used in Figure 1: DB, Dolphin Bay; SK, Shark Hole; RA, Rana Azul; PO, South Popa; CL, Colón; BW, Bastimentos West; HP, Hospital Point; PD, North Popa; SC, San Cristóbal; and TB, Tranquilo Bay.

To further investigate the timescale of migration and the split between populations, we performed demographic inference for pairs of populations using dadi.[49] Assuming a mutation rate of 10^{-9} bp per year,[50,51] the divergence time between populations predates all of the island formation times (Table 1). For example, Isla Colón and Isla Bastimentos separated ~5,200 years ago.[4] Our results suggest the split time between the two closest (genetically and geographically) populations, CL and BW, was ~44,000 years ago (Table 1). This suggests that these morphs arose either through drift or selection on standing genetic variation that predates the current-day configuration of these islands.

Distinct carotenoid compositions between color morphs

We analyzed the carotenoid composition of dorsal skin in *O. pumilio* morphs using high-performance liquid chromatography (HPLC) and found differences in carotenoid concentrations among color morphs (Table S2; Figure 2). Overall, the skin of red and orange morphs had the highest total carotenoid content, while green and yellow frogs displayed intermediate levels. By contrast, blue frogs were almost entirely devoid of carotenoids.

To better understand variation in carotenoid composition, we grouped morphs based on their similarities (Figure 2; Table S2). Red and orange frogs contained high concentrations of all carotenoid types, with the main difference being that orange frogs had higher levels of β-carotene and colorless apocarotenoids but lower red ketocarotenoid content. However, no pigment was completely absent in either group. Green and yellow morphs, particularly CL-G and BW-Y, had similar carotenoid profiles (Figure 2A). HPLC analysis of a CL-G individual revealed a complete absence of red ketocarotenoids (Figure 2D). Blue frogs, on the other hand, exhibited a drastically different carotenoid composition, being almost completely without carotenoids except for colorless apocarotenoids and a few dietary yellow pigments (Figure 2E).

To assess the significance of these differences, we performed a SIMPER test in R using the *vegan* package.[52] Due to small sample sizes, we grouped morphs into three categories for analysis: (1) red/orange (n = 5), (2) yellow/green (n = 4), and (3) blue (n = 2), excluding the intermediate/brown DB morph. We found that red ketocarotenoids and dietary orange carotenoids were significantly more abundant in red/orange frogs compared with yellow/green frogs. Additionally, colorless apocarotenoid content differed significantly between yellow/green and blue morphs, with higher content of apocarotenoids in blue frogs (Table S2).

Finally, we examined the relationship between carotenoid concentrations and spectrometric color measurements. Apocarotenoid concentration correlated negatively with green wavelength brightness measurements, while β-carotene concentration showed a positive linear relationship with red hue and brightness (Table S3).

Genomic basis of skin color variation

Blue

To uncover the genomic basis of blue coloration, we sampled blue frogs from RA-B, DB-B, and SK-B. Since DB is a polymorphic blue population, also harboring red and intermediate phenotypes with very low genome-wide divergence between morphs (F_{ST} = 0.01), we would expect that by performing an F_{ST} scan along the genome, we would detect a highly divergent region between sympatric morphs. Adding an outgroup allows us to detect which of the morphs is diverging from the ancestral form. We performed a window-based (size = 100,000 bp; step = 20,000 bp) population branch statistic (PBS) scan, which is analogous to a three-way F_{ST} scan, comparing the DB-B and DB-R, using the TB-R population as an outgroup. The most differentiated gene between red-blue morphs was found in the blue frogs (DB-B) and is *kit* (Figures 3A–3C). The *kit* gene is contained within

Please cite this article in press as: Aguilar-Gómez et al., Selection-driven color variation in the aposematic strawberry poison frog, *Oophaga pumilio*, Current Biology (2026), https://doi.org/10.1016/j.cub.2026.01.041

CellPress
OPEN ACCESS

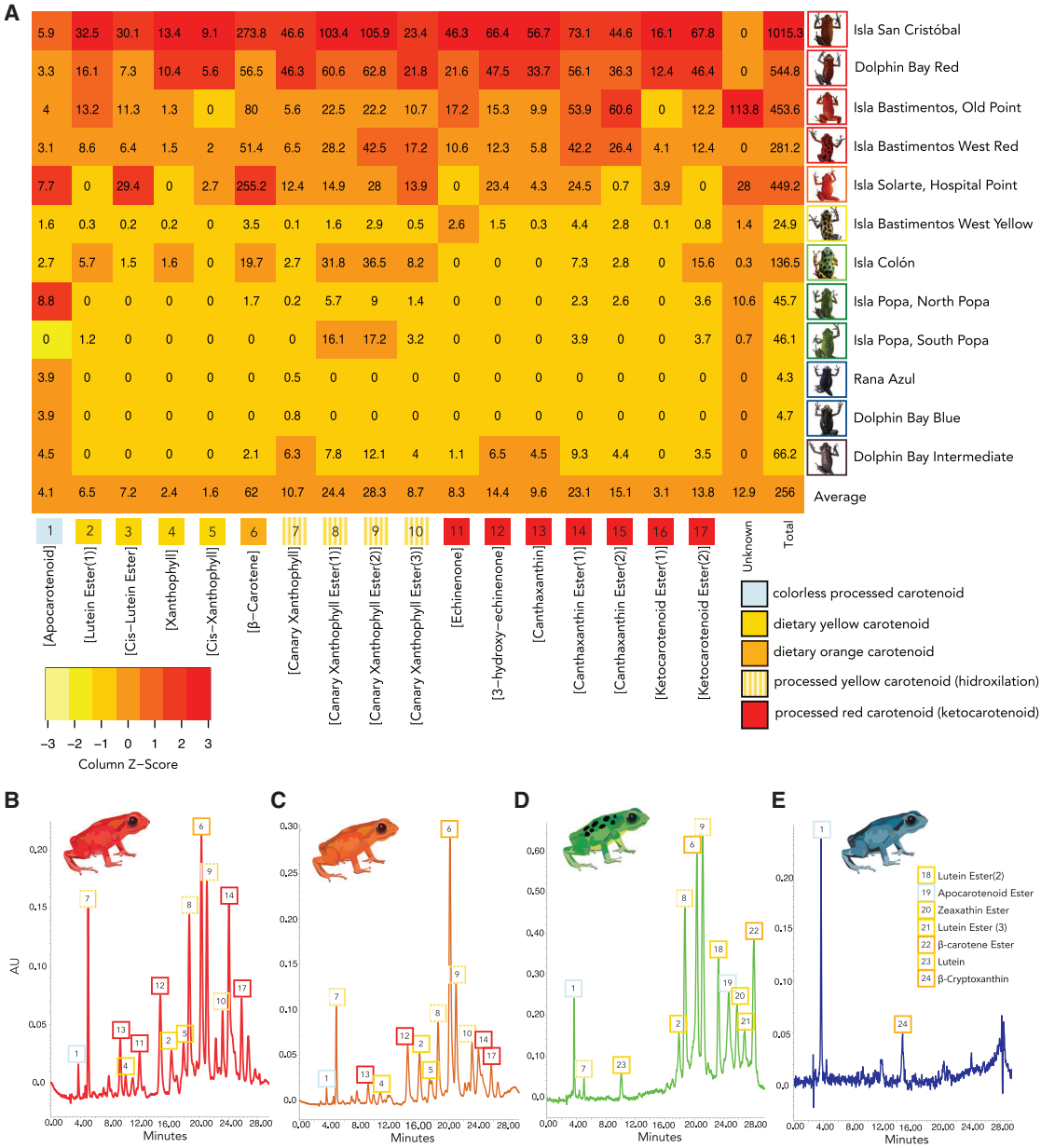

Figure 2. Carotenoid composition in skin of *O. pumilio* color morphs

(A) Carotenoid content in different morphs. The dorsal color of the morphs is shown in squares to the left of the names. On the *x* axis, carotenoids are numbered in squares and colored according to the type of carotenoid. The heatmap shows pigment concentrations (ng/g), and the color of each cell corresponds to deviations from the mean concentration across all samples (*Z* score). Note that values are not normally distributed, and *Z* scores are used here solely for visualization.

(B) Two-dimensional HPLC chromatogram showing the carotenoid composition of a representative red morph individual (Almirante, mainland). Here and below, peaks are labeled with numbers corresponding to those in (A).

(C) Chromatogram showing the carotenoid composition of a representative orange morph individual (HP).

(D) Chromatogram showing the carotenoid composition of a representative green morph individual (CL).

(E) Chromatogram showing the carotenoid composition of a representative blue morph individual (RA).

See also Tables S2 and S3.

a single outlier 100 kb window. Adjacent overlapping windows (20 kb step) did not surpass the threshold, and no other genes are located in this region. Kit is a tyrosinase kinase receptor involved in melanocyte precursor expansion, survival, proliferation, and migration.[53] This gene has a role in coloration in other systems.[54,55] Kit ligand (*kitlga*) binds to Kit to activate it and has also been associated with multiple color and pattern phenotypes.[55–57] In particular, *kitlga* is linked to red-blue polymorphism in betta fish.[58] Overexpression of *kitlga* can affect size and number of melanocytes, leading to hyperpigmentation.[59]

Please cite this article in press as: Aguilar-Gómez et al., Selection-driven color variation in the aposematic strawberry poison frog, *Oophaga pumilio*, Current Biology (2026), https://doi.org/10.1016/j.cub.2026.01.041

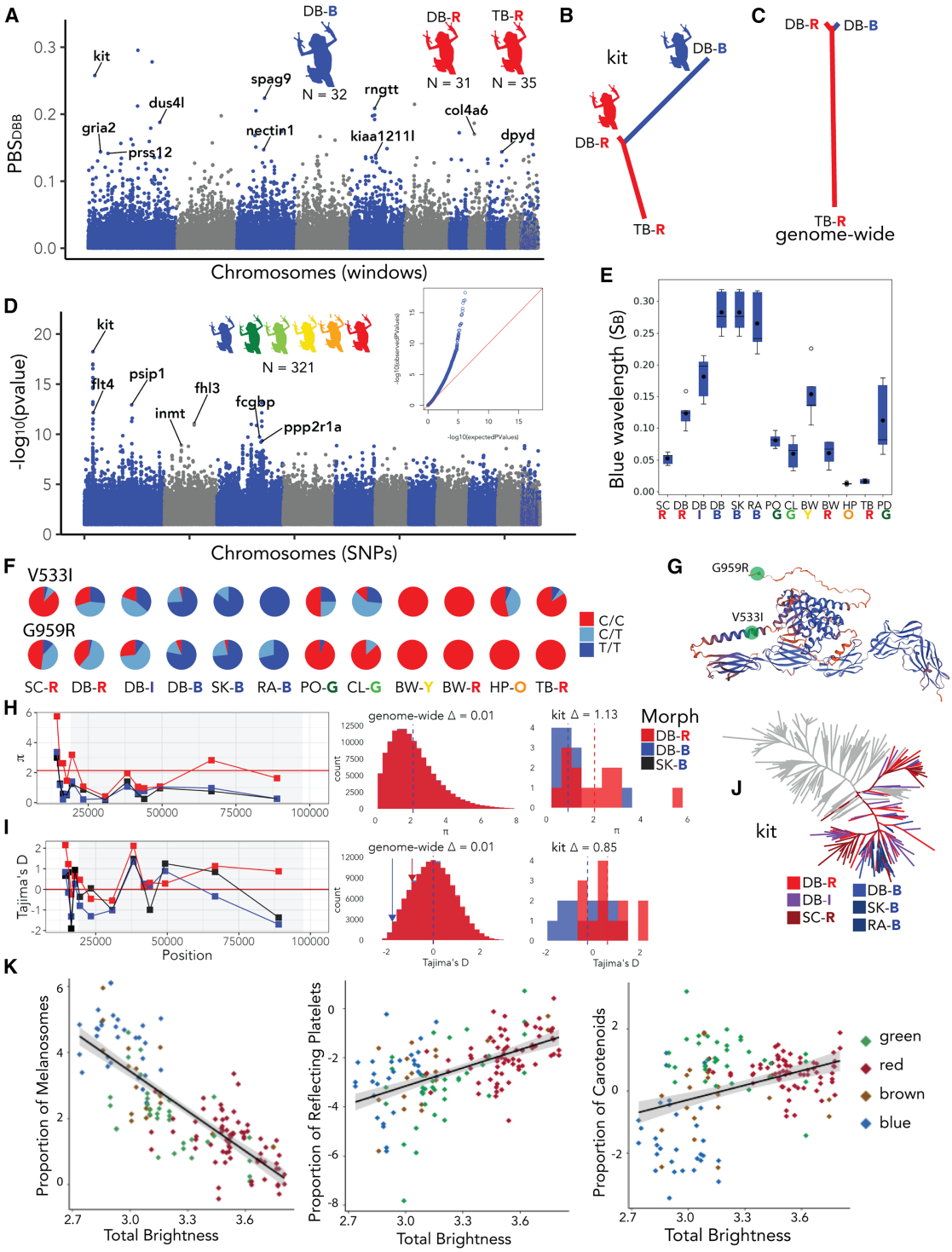

Figure 3. Genetic basis of blue coloration in *O. pumilio*

(A) PBS scan of Dolphin Bay blue (DB-B) branch against DB-R and TB-R. Mapped to *O. pumilio*, the plot using synteny, alternating colors are chromosomes from *O. sylvatica*.

(B) PBS tree of *kit* scaffold.

(C) PBS genome-wide.

(D) Genomic association to reflectance at blue wavelengths using unrelated individuals. The horizontal axis shows the position of every SNP that was included in the GWAS with respect to *O. sylvatica* synteny. The vertical axis is the negative logarithm (base 10) of the *p* value (−log10(*p* value)) of the association.

(E) Blue wavelength (SB) measurements grouped by population, with measurements on five individuals per morph.

(legend continued on next page)

Please cite this article in press as: Aguilar-Gómez et al., Selection-driven color variation in the aposematic strawberry poison frog, *Oophaga pumilio*, Current Biology (2026), https://doi.org/10.1016/j.cub.2026.01.041

We also conducted a GWAS using reflectance measures at blue wavelengths across all morphs (Figure 3D), analyzing only unrelated individuals (n = 321) and using imputed population-average phenotypes (Figure 3E), while correcting for population structure using a relatedness matrix. Again, the gene with the strongest association with blue wavelengths was *kit*. We identified two non-synonymous mutations in *kit*: V533I and G959R. V533I is located in the transmembrane domain of Kit. This mutation is fixed for the ancestral allele in BW, has a higher frequency in darker populations (Figure 3F), and explains 4.5% of the phenotypic variance among populations. Meanwhile, G959R, located in the C-terminal domain of Kit (Figure 3G), is fixed for the ancestral allele in bright populations such as TB-R, BW-Y/BW-R, and HP-O, but instead segregates in DB and in duller/darker colored populations (Figure 3F). This mutation explains 11% of the phenotypic variance among populations. Encouragingly, a previous expression study also identified mutations unique to blue frogs in the *kit* gene.[43] The SNP within *kit* that explains the most variance among populations is a synonymous mutation located in an exon (scaffold31043:53032, adjusted p = 9.15e–23) and explains 13% of the variance. We note that, for any of these mutations, we cannot make causal inferences, and the amount of variance explained might be affected by linkage disequilibrium (LD) with other variants.

The morphs differ in the thickness of the dermis (the layer of the skin where pigments are found) and in the total number of pigment cells per unit area. As such, rather than quantifying the different types of pigment-containing cells separately, we compared the relative proportions of different pigments in the skin. Interestingly, we found that blue *O. pumilio* have a higher proportion of melanosomes (containing black pigments) compared with red and green frogs (Figure 3K). A *kit*-driven alteration in melanosome composition could explain shifts in pigment proportions, leading to structural blue coloration. The *kit* allele present in blue frogs likely enhances melanin production, increasing melanosome density and contributing to their darker skin. Histological sections of blue frogs show an increased density of melanophores, a reduction in xanthophores, and a similar overall abundance of iridophores compared with red morphs (Figure S2). However, a key difference lies in the spatial arrangement of these chromatophores: in blue frogs, melanophores occur closer to the epidermis, altering the layering between pigment cells and reflecting platelets. Although iridophores do not appear reduced in absolute number, their platelets may be proportionally fewer relative to other pigments (Figure 2K) and are positioned under melanophores instead of above them. Because iridophores produce blue-green coloration when spatially close to melanophores but tend to reflect longer wavelengths, such as red, when isolated,[61] this altered layering and proportion in blue frogs results in closer interaction of melanin and reflecting platelets, consistent with blue structural coloration. By contrast, brighter populations, such as BW, where *kit* is fixed for the reference allele, have fewer melanosomes (Figures 3K and S2), contributing to their lighter coloration.

In the genome-wide tree, individuals from the DB polymorphic population do not cluster by color (Figure S1). However, in the *kit* gene tree, most of the blue frogs from DB (28 of 32) cluster with the remaining blue frogs from the Aguacate Peninsula (34 of 37; SK and RA), in a clade distinct from the red frogs from DB (Figure 3J).

To investigate selection acting on *kit*, we compared local values of average pairwise differences (π) and Tajima's D to genome-wide values in DB. The blue morph has reduced variability and low values of Tajima's D, suggesting a selective sweep in this morph (Figures 3H and 3I). We also performed an HKA test to determine if the ratio of polymorphism within morphs to divergence between morphs in our candidate genes was consistent with genome-wide values. DB-B frogs have relatively fewer polymorphic sites in *kit* than DB-R frogs. SK, the monomorphic blue population, has significantly fewer polymorphic sites in *kit* ($q < 0.05$), supporting the hypothesis of a selective sweep (Table S4).

Yellow, orange, and red

Vertebrates cannot produce carotenoids, the pigments that produce yellow, orange, and red coloration, and instead must obtain them through their diet.[32] The only yellow morph in Bocas del Toro is in BW-Y. There is very little genetic differentiation between yellow and red color morphs on BW, as their genome-wide F_{ST} is very low (~0.01; Table S1). However, a few genes have very different allele frequencies between morphs. Some SNPs show extremely high differentiation (F_{ST} = 0.98), and even when averaged across 100 kb windows (step = 20 kb), F_{ST} remains elevated (>0.2; not shown). To identify which branch contributes to this differentiation between the morphs, we calculated PBS using an outgroup, revealing regions with particularly high PBS_{BMY} values (>0.4; Figure 4A). Among these genes, we identified *ttc39b*, *tyrp1*, *psip1*, *zdhhc21*, *frem1*, and *nfib*. This group of genes was initially described to be located in the mouse brown locus (its mutation causes albino phenotypes), which contains the known pigmentation genes *tyrp1* and *bnc2*.[62] In the fragmented *O. pumilio* assembly,[43,46] the genes are on different scaffolds, but we note that they are also in the same syntenic region of the high-quality *O. sylvatica* genome, suggesting that the synteny is conserved across tetrapods and that these F_{ST} outliers represent the same divergence signal.

We used the blue population RA-B as an outgroup in a PBS scan between the BW populations (BW-R and BW-Y) to determine which morph contributed to the observed allele frequency

(F) Allele frequency of non-synonymous mutations of *kit*.
(G) Structure of Kit in *O. pumilio* generated with *SWISS-MODEL*.[60] Non-synonymous mutations are highlighted in green.
(H) Pairwise differences (π) in windows containing 1,000 sites (variant and invariant) that pass all quality filters in the *kit* scaffold. The shaded area contains the protein-coding region. Blue squares correspond to DB-B, red to DB-R, and black to SK-B. Horizontal lines indicate genome-wide averages (red, DB-R; blue, DB-B), and the blue line lies directly beneath the red line and thus is not visible. To the right, overlaid histograms of the distributions of pairwise differences, from left to right: genome-wide and within the gene *kit*. Morph differences are shown above each histogram (Δ).
(I) Tajima's D presented in the same format as (H). Arrows in the genome-wide histogram show the location of the window with the smallest Tajima's D value.
(J) Gene tree of *kit*. Mainland populations and SC are colored according to dorsal coloration of the frog, and all other island individuals are in gray.
(K) Proportion of pigments in different color morphs of *O. pumilio*, reproduced from Freeborn.[45]
See also Figures S2 and S3, Tables S4–S6, and Data S2.

Please cite this article in press as: Aguilar-Gómez et al., Selection-driven color variation in the aposematic strawberry poison frog, *Oophaga pumilio*, Current Biology (2026), https://doi.org/10.1016/j.cub.2026.01.041

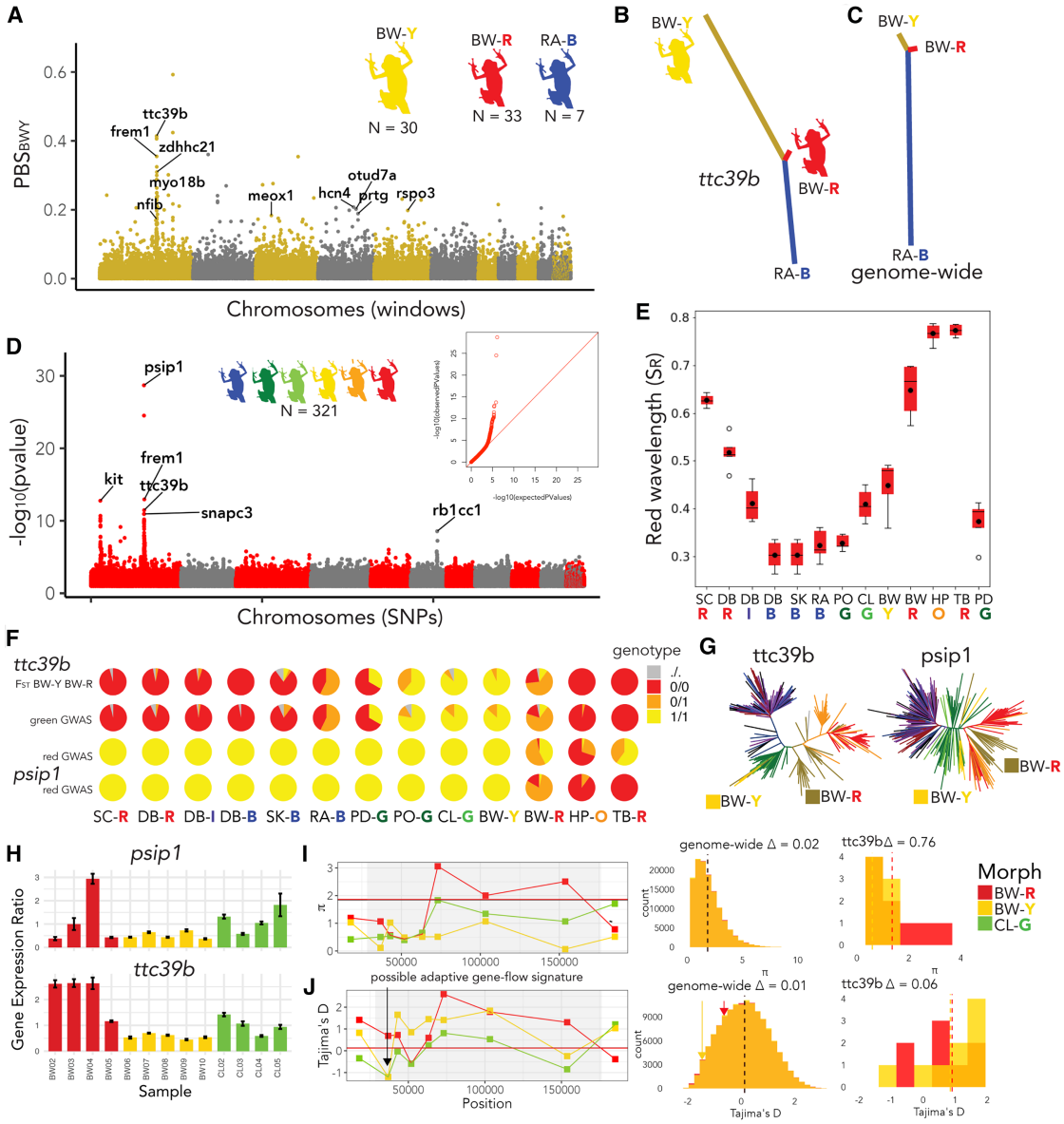

Figure 4. Genetic basis of yellow/red coloration in *O. pumilio*

(A) PBS scan of BW-Y branch against BW-R and RA-B.

(B) PBS tree of *ttc39b* scaffold.

(C) PBS genome-wide.

(D) Genomic association to reflectance measurements at red wavelengths using unrelated individuals. The horizontal axis shows the position of every SNP that was included in the GWAS with respect to *O. sylvatica* synteny. The vertical axis is the negative logarithm (base 10) of the *p* value (−log10(*p* value)) of the association.

(E) Red wavelength (SR) measurements grouped by population, with measurements on five individuals per morph.

(F) Allele frequency of SNPs in *ttc39b*: P_RNA_scaffold_17998:28559, the highest F_{ST} BWY-BWR value (F_{ST} = 0.98); P_RNA_scaffold_17998:47512, the top *ttc39b* SNP in the green GWAS; P_RNA_scaffold_17998:71352, the top *ttc39b* SNP in the red GWAS; and in *psip1*−. P_RNA_scaffold_10726:251470, the top SNP in the red GWAS.

(G) Gene trees, colored according to Figure 1A: BW-Y (yellow), BW-R (gold), CL-G (light green), PP-G (dark green), and TB-R (red).

(H) qPCR results showing gene-expression ratio of housekeeping gene *sdha* and *ttc39b*.

(I) Pairwise differences (π) in windows containing 1000 sites (variant and invariant) that pass all quality filters in the *ttc39b* scaffold. The shaded area contains the gene *ttc39b*, and yellow squares correspond to BW-Y, red to BW-R, and green to CL-G. Horizontal lines indicate genome-wide averages (red, BW-R; black, BW-Y), and the black line lies directly beneath the red line and is not visible. To the right, overlaid histograms of the distributions of pairwise differences, from left to right: genome-wide and within the gene *ttc39b*. The vertical dashed lines represent the means of the distributions (BWR, red; BWY, black).

(J) Tajima's D presented in the same format as (I).

See also Figure S3, Tables S4 and S5, and Data S2.

Please cite this article in press as: Aguilar-Gómez et al., Selection-driven color variation in the aposematic strawberry poison frog, *Oophaga pumilio*, Current Biology (2026), https://doi.org/10.1016/j.cub.2026.01.041

changes. We found a sharp peak in the BW-Y PBS branch (Figures 4A and 4B). The BW-Y branch is 70 times longer in *ttc39b* than genome-wide (genome-wide = 0.00567, *ttc39b* = 0.414; Figures 3B and 3C). *Ttc39b* is the gene with the highest BW-Y PBS value between yellow and red frogs of the polymorphic BW population. This gene is involved in carotenoid-based phenotypes in fish and birds.[63–66] It was also found as a candidate gene with differential expression between different color morphs of other dendrobatids.[67] In birds, *ttc39b* enhances the conversion of dietary yellow carotenoids into red ketocarotenoids,[32] with recessive mutations in *ttc39b* resulting in yellow phenotypes.[68] Our results suggest this mechanism might be conserved in frogs.

We conducted a GWAS across all populations using reflectance measures at red wavelengths. The lowest *p* values were observed in *psip1*, *snapc3*, *frem1*, and *ttc39b* (Figures 4D and 4E), all located within the same genomic region. We chose to focus on *psip1*, which showed the strongest association in the GWAS, and *ttc39b*, which exhibited the greatest divergence among morphs. Examining the SNPs with the smallest *p* values in *ttc39b* and *psip1*, we found alleles that were fixed in most populations but segregating in HP-O, TB-R, and BW-Y/BW-R. These SNPs explain 29% and 7.5% of the variance among populations (genetic + environmental + measurement), respectively. The second peak in the GWAS is in *kit* (Figure 4D), and its top SNP explains 5% of the variance. As this GWAS was done measuring reflectance at red wavelengths using all morphs, the presence of the two peaks might suggest that variants in both regions are needed to produce red coloration, with alternative haplotypes in each of those genomic regions resulting in non-red morphs.

We also identified a highly differentiated SNP between BW morphs (F_{ST} = 0.98) within the scaffold containing *ttc39b*. Most yellow morphs in BW carry the alternative allele, which is also present in green frogs (Figure 4F). Given *ttc39b*'s known role in carotenoid metabolism—specifically enhancing the conversion of yellow to red pigments[32]—mutations in or near this gene may underlie the loss of red pigmentation. While we did not detect highly differentiated non-synonymous mutations, we identified several intronic SNPs with striking allele frequency differences between color morphs (Figure 4F), suggesting a regulatory mechanism. Supporting this, *ttc39b* was differentially expressed in BW morphs, with red frogs showing higher expression (Figure 4H). Since red is the ancestral coloration in *O. pumilio*,[35] and non-red individuals predominantly carry the alternative allele in the homozygous state, this suggests reduced *ttc39b* function in non-red morphs. Previous pedigree studies showed that color variation in BW is largely determined by a single locus, with red dominant over yellow.[14] Our findings strongly suggest this locus is *ttc39b*.

Although the genome-wide phylogenetic tree does not separate yellow and red individuals in BW, the *ttc39b* gene tree distinctly clusters yellow individuals with green frogs from CL, PO, and PD (Figure 4G). That the *ttc39b* yellow haplotype clusters solidly within green frog haplotypes suggests that there is shared ancestry between the haplotype associated with yellow coloration in BW and the one found in green frogs from CL, PO, and PD. Furthermore, the estimated time to coalescence of *ttc39b* between the red and yellow morphs of BW is much greater (~1.7 million years ago [mya]) than the divergence times among different Bocas del Toro populations (all <80,000 years; Table 1), suggesting that the yellow haplotype arose prior to the formation of the islands.

To assess selection at this locus, we compared π and Tajima's D to genome-wide levels. The yellow morph exhibited low π and a wide range of values for Tajima's D (Figures 4I and 4J), with a dip around position 36,816. In fact, the window covering positions 35,487–38,145 fall within the lowest 6% of Tajima's D values and the lowest 3% of π values in BW-Y. Furthermore, in that window, the difference between the values for the red and the yellow morph is among the 96% and 99.6% most extreme in the genome. Tajima's D, and to a certain degree π, increase starting at ~40,000 bp from the extreme dip, and both the yellow and red morphs have increased values of Tajima's D in the flanking regions, which is compatible with selection acting on a haplotype that entered the population by admixture.[69,70] The low values of Tajima's D and reduced values of π in this region also conflict with hypotheses of long-standing local balancing selection on Bastimentos as a mechanism to maintain the polymorphism. An HKA test further supports selection in the yellow morph, revealing fewer polymorphic sites within BW-Y ($q < 0.05$; Table S4).

The clustering of the BW-Y *ttc39b* haplotype with green populations (CL-G and PO-G; Figure 4G) suggests it was introduced to BW via admixture and subsequently increased in frequency due to continued positive selection. This is consistent with Admixture Bayes results, which indicate gene flow between the ancestors of CL and BW (Figures 1E and S1).

Green

Identifying the genetic basis of green coloration was more challenging due to the absence of a polymorphic green population. This challenge is compounded by the fact that amphibians do not possess a green pigment per se. Rather, green coloration is generally produced by the combination of yellow pigments and blue structural coloration.[34] To investigate this, we performed a GWAS using reflectance measures at green wavelengths and found *ttc39b* and *psip1* at the lead association peak (Figures 5A and 5B), although SNPs near *psip1* had smaller *p* values. Gene trees for *ttc39b* and *psip1* (Figure 4G) suggest that yellow and green frogs share similar alleles at these loci. Additionally, green frogs from CL, PO, and PD have yellow venters (Figure S2), supporting the hypothesis that one component of green coloration is yellow pigmentation, inherited via a haplotype shared with the yellow BW-Y population.

Previous research on *ttc39b* and its involvement in carotenoid conversion, along with our expression results (Figure 4H), suggests that *ttc39b* plays a major role in green coloration, as both green and yellow frogs have lower expression of *ttc39b* compared with red frogs. However, a causative role for *psip1* cannot be excluded. Interestingly, the top SNP in *psip1* is the same as that identified in the red GWAS and explains 33% of the variance in green coloration among populations. Meanwhile, the top SNP in *ttc39b* explains 18% of the variance and exhibits a similar allele frequency distribution across all morphs as the most differentiated SNP among Bastimentos morphs (Figure 4F).

We conducted PBS scans focused on the branches of the two independent green frog populations, CL-G and PO-G, comparing

Please cite this article in press as: Aguilar-Gómez et al., Selection-driven color variation in the aposematic strawberry poison frog, *Oophaga pumilio*, Current Biology (2026), https://doi.org/10.1016/j.cub.2026.01.041

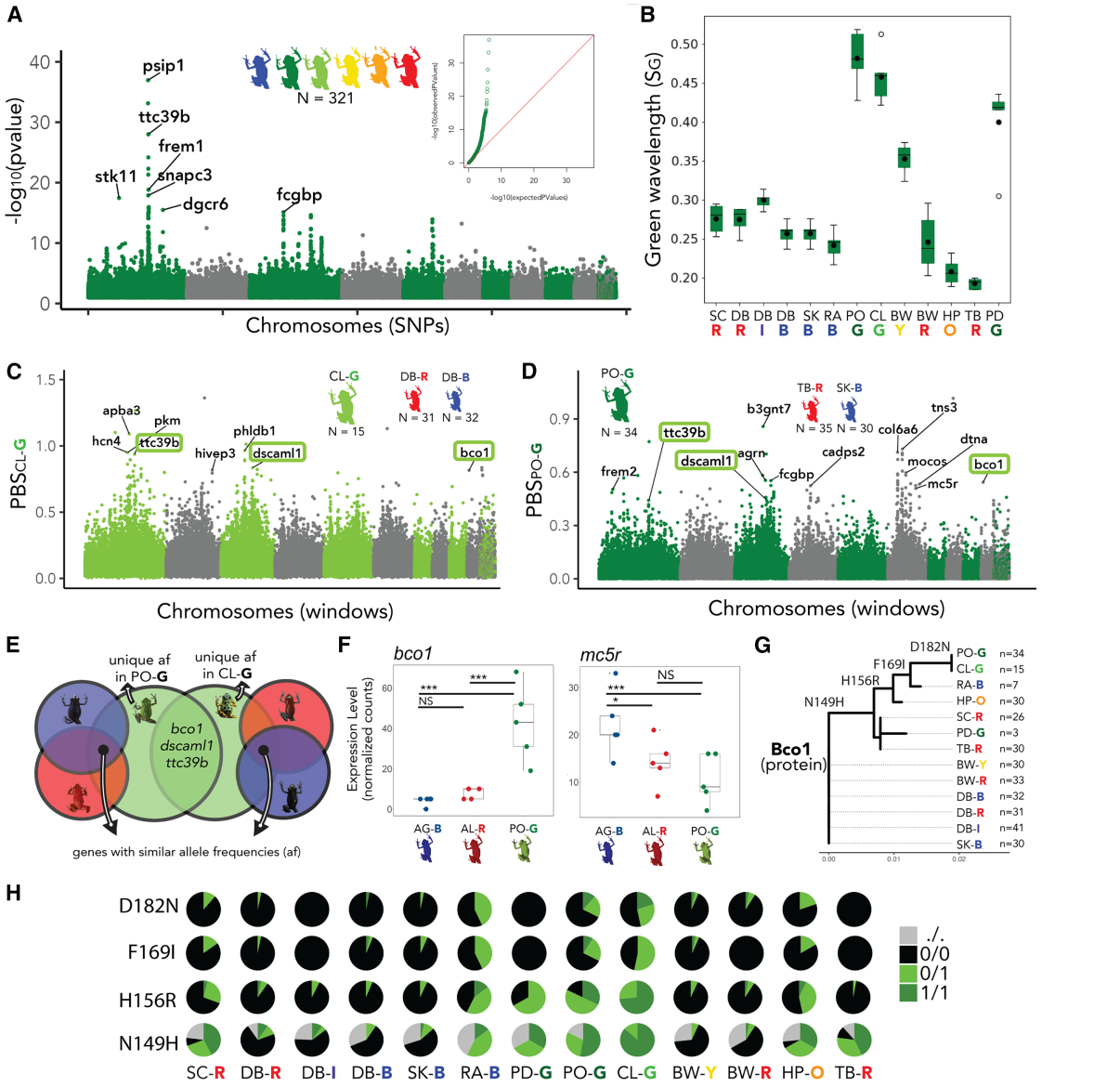

Figure 5. Genetic basis of green coloration in *O. pumilio*

(A) Genomic association to reflectance measurements at green wavelengths using unrelated individuals. The horizontal axis shows the position of every SNP that was included in the GWAS with respect to *O. sylvatica* synteny. The vertical axis is the negative logarithm (base 10) of the *p* value (−log10(*p* value)) of the association.

(B) Green wavelengths (SG) measurements grouped by population, with measurements on five individuals per morph.

(C) PBS scan of the CL green branch against DB-B and DB-R.

(D) PBS scan of PO green branch against SK-B and TB-R.

(E) Venn diagram of the strategy for finding genes differentiated in green frogs.

(F) Differential expression of *bco1* and *mc5r* in different color morphs. Adjusted *p* value significance levels are shown as $*p < 0.05$, $***p < 0.005$; non-significant (NS).

(G) Tree of Bco1 (protein) made with consensus sequence per population.

(H) Non-synonymous mutations found in *bco1*.

See also Figure S3, Table S5, and Data S2.

them to non-green morphs. Since some of the genetic basis for green seems to be at least partially shared with yellow frogs, we chose one red and one blue outgroup to maximize the ability to detect a pattern specific to green. To minimize the noise, we chose the least diverged (Table S1) red and blue populations relative to each green population: (1) a PBS analysis of CL-G versus DB-B and DB-R (Figure 5C) and (2) of PO-G versus SK-B and TB-R (Figure 5D). In addition to *ttc39b*, the only other genes we found as outliers in both scans were *bco1* and *dscaml1* (Figure 5E). *Dscaml1* is expressed in rods, rod bipolar cells, and subsets of amacrine cells (interneurons in the retina that modulate visual signals). Its disruption has been linked to congenital

Please cite this article in press as: Aguilar-Gómez et al., Selection-driven color variation in the aposematic strawberry poison frog, *Oophaga pumilio*, Current Biology (2026), https://doi.org/10.1016/j.cub.2026.01.041

stationary night blindness, suggesting this gene may play an important role in vision.[71] Notably, at least one study has reported differences in visual sensitivity among *O. pumilio* color morphs, including comparisons between red and green morphs, raising the possibility that variation in this gene could be associated with morph-specific visual differences.[72]

Bco1 is *beta-carotene oxygenase 1*, a gene that cleaves beta-carotenoids (dietary yellow and orange carotenoids) into smaller, often colorless apocarotenoids.[73,74] Expression of *bco1* is markedly higher in green frogs (Figure 5F) compared with red and blue morphs. To investigate its evolutionary history, we estimated haplotype divergence times in *bco1* between green and red morphs (CL-G versus DB-R; PO-G versus TB-R). Both comparisons yielded similar results, with an average coalescence time of ~2 mya—substantially older than the divergence times among Bocas del Toro populations (Tables 1 and S5). Remarkably, the green haplotype predates the formation of the islands and is the oldest haplotype we identified across all candidate genes. In addition, we generated a tree using the consensus sequence for each of the populations (Figure 5G) and detected four non-synonymous mutations segregating within *bco1*, with the alternative alleles occurring at higher frequency in green frogs (Figure 5H), further supporting the conclusion that this haplotype is ancient. *Bco1* has been previously reported in color variation in ornamental betta fish,[58] and its paralog *bco2* has been found to be involved in multiple color phenotypes.[75–78] One of the challenges of the *bco1* region for our analysis is that it has missing data. Several key SNPs did not meet the minimum quality thresholds required for inclusion in the GWAS, which prevented site-specific tests at this locus. As a result, the gene could only be identified through a window-based approach. Because green coloration results from the combination of yellow pigmentation and blue structural coloration, some overlap in genes between yellow and green morphs is expected (e.g., *ttc39b*). By contrast, genes such as *bco1*, which appear to be specifically associated with green, would not necessarily be expected to be detected in the yellow morph, as green coloration is not required to produce yellow.

Other interesting outlier genes in either green PBS scan are *frem2*, *mc5r*, *fcgbp*, and *col6a6* (Figures 5C and 5D). *Mc5r* is one of the five genes in the family of melanocortin receptors found in most vertebrates.[79] This gene is expressed in melanophores and xanthophores and has a role in pigment dispersion.[80–83] *Mc5r* is differentially expressed in different morphs of *O. pumilio* (Figure 5F). *Frem2* has been implicated in melanophore development.[84] *Fcgbp* has not been functionally found in pigment pathways but was one of the few genes identified to show strong evidence of selection in polar bears (with pigment-free fur) compared with brown bears (with brown fur), indicating a potential role in pigmentation.[85] We found this gene associated with reflection of green wavelengths (Figure 5A), with its top SNP explaining 17% of the variance. Collagen gene *col6a6* was found as an outlier in multiple PBS analyses: in the green branch of PO-G, SK-B, and TB-R (Figure 5D), in the blue branch of SK-B, PO-G, and TB-R (Figure S3), and in the orange branch of HP-O, CL-G, and PO-G (Figure S3). Collagen is important for skin color and its reflective properties in frogs.[45] The thickness of the collagen layer differs between different morphs of *O. pumilio*, and red frogs have significantly thicker collagen layers than blue frogs.[45] Thus, our finding of a collagen gene such as *col6a6* in many different comparisons among morphs could indicate that the gene plays a role in color variation through changes in collagen layer thickness.

We identified additional pigmentation-associated genes as outliers across multiple PBS scans. In the comparison between green and orange frogs, the orange morph exhibited a longer branch for the gene *scarb1*, a known carotenoid gene (Figure S3).[43,63,86] Several keratin genes (*krt10*, *krt12*, *krt14*, *krt17*, and *krt24*) were found as outliers in red frogs[67] (Figure S3). We also found *gnpat*, *adamts8*, and *lyst* as outliers in the blue frogs (RA-B) compared with BW populations (Figure S3). *Gnpat* has an adaptive variant in humans that promotes melanin synthesis in Tibetans as an adaptive mechanism against UV radiation, making their skin darker.[87] *Lyst* has been repeatedly implicated in pigmentation variation, with mutations producing lighter skin or coat color phenotypes across diverse vertebrate taxa, including mammals and reptiles.[88–91] Although *adamts8* has not been directly linked to pigmentation, several of its paralogs, such as *adamts9*,[92] *adamts13*,[93] and *adamts20*,[84,94] play known roles in chromatophore differentiation and migration.

DISCUSSION

In this study, we identified several candidate genes responsible for color differences in the extremely variable morphs of *O. pumilio* from Bocas del Toro, Panama. For blue frogs, the strongest candidate is *kit*, which harbors two non-synonymous candidate mutations (V533I and G959R). Using the consensus sequence for the gene in each population (Figure S2), we found that the brighter morphs, like yellow, orange, and red, on average, do not have any of these mutations. V533I is present in darker morphs like green, blue, and red morphs from DB, which are probably better described as burgundy (darker red) and have blue ventral coloration. G959R is only predominant in blue frogs. The amino acid changes in the same position in humans are associated with cancer, as are most described mutations in this gene.[95] More interestingly, a mutation in the C-terminal domain makes it more amphipathic, resulting in piebaldism (white patchiness where melanin is missing; Table S6).[96] The *O. pumilio* mutation G959R in the C-terminal domain increases hydrophobicity, potentially having the opposite effect, increasing Kit activation and melanization. This hypothesis is compatible with our finding that blue frogs have more dermal melanosomes. A sweep in this gene and association with both blue and red wavelengths supports the hypothesis that this is a key gene that differentiates red frogs from blue. In addition, blue frogs lack pigmented carotenoids. They display only colorless apocarotenoids, and histological sections show differences in chromatophore organization, including melanophores located closer to the epidermis in blue frogs. Collectively, these genomic, biochemical, and histological observations support the hypothesis that alterations in Kit and associated pigmentation pathways contribute to the distinct blue coloration in *O. pumilio*.

It was previously hypothesized, based on segregation patterns in pedigrees, that a single locus dominant for red was responsible for the yellow/red phenotypic polymorphism in the BW population.[14] Our analyses suggest that this locus includes *ttc39b*, a gene that enhances the conversion of dietary yellow

Please cite this article in press as: Aguilar-Gómez et al., Selection-driven color variation in the aposematic strawberry poison frog, *Oophaga pumilio*, Current Biology (2026), https://doi.org/10.1016/j.cub.2026.01.041

carotenoids into red ketocarotenoids.[32] Our HPLC results support this hypothesis, with yellow and green frogs having very low content of ketocarotenoids (Figure 2). The haplotype is shared between yellow frogs from Bastimentos and green frogs from Isla Colón and Isla Popa. The fact that the yellow Bastimentos haplotype (BW-Y) is positioned within the green flog clade (CL-G + sylvaticPO-G + PD-G) in the haplotype tree for *ttc39b*, but not in the genomic tree, suggests that the haplotype was introduced by migration from Isla Colón into Isla Bastimentos (Figure 4G). We identify recent selection occurring in BW with very few genetic polymorphisms within the yellow frogs. A similar pattern of low variation in *ttc39b* is also observed in the CL-G (Table S4), which is compatible with the hypothesis that selection might have acted in green frogs first before the transfer of the haplotype to Isla Bastimentos. In addition, the surrounding region shows extended LD and multiple outlier genes, raising the possibility that other loci, or even an undetected structural variant such as an inversion, could also contribute to the phenotypic differences.

Another important gene with several non-synonymous mutations and higher expression in the green morphs is *bco1*. We hypothesize that this gene is changing the carotenoid content in green frogs compared with frogs with other colors. By quantifying the different pigments and reflecting platelets, we provide evidence that both blue and green morphs in *O. pumilio* are produced, at least partly, through structural coloration. Blue frogs are produced through a change in light absorbance via an increased number of melanosomes (Figure 3K), and green frogs are produced via different content of carotenoids (Tables S2 and S3). Bco1's function is to cleave longer carotenoids into colorless apocarotenoids, and the observed differences in types of carotenoids can be explained by the divergence of this gene in the different color morphs and the higher levels of expression in green morphs. The absence or low concentration of red ketocarotenoids in yellow and green morphs, compared with red/orange, supports the role of *ttc39b*—a gene under selection with extreme allele frequency differences between morphs—as a major contributor to skin color variation. Carotenoid processing may be key to explaining the differences between *O. pumilio* color morphs. However, detailed functional studies would be needed to confirm the mechanism of action of the associated genes identified in this study.

Many hypotheses involving both selective and neutral evolutionary processes have been proposed regarding the origin and maintenance of color variation in *O. pumilio* in Bocas del Toro.[15,17,28] We propose a morph pump dynamic model, a process that maintains high degrees of polymorphism over long periods of time. The original idea comes from the "species pump" hypothesis with cycles of island connectivity and isolation.[97] The islands of Bocas del Toro have been connected and reconnected throughout the history of sea level fluctuations stemming from past changes in global climate.[98] Our demographic models suggest that the populations started diverging before the current iteration of the islands formed, implying that the variation that we observed in the islands could have been segregating in *O. pumilio* before the populations split. Our calculations of haplotype divergence between genes of interest suggest that all of them predate the current-day configuration of the archipelago (Tables 1 and S5).

We find selection signatures in some of our candidate genes. In particular, we find a signal of recent selection on the introduced haplotype of the *ttc39b* gene associated with yellow color in the polymorphic population from Bastimentos. This demonstrates that novel phenotypes can be selected for within islands after island formation. We find similar evidence of selection associated with the blue phenotype in the polymorphic DB region of mainland Panama. This suggests that the evolution of new morphs is not necessarily associated with the formation of the islands but instead can be driven by local selection. It also raises two new questions. First, what is the source of this selection? And second, why is its influence limited to the Bocas del Toro area?

While this study cannot identify the source of selection on color, previous results suggest that male-male competition, female mate choice, or viability selection are possible explanations.[6,7,13,22,99] Male-male competition and female mate preferences have been shown to be color-assortative, which, in the case of male-male competition, provides a mechanism for selection to favor rare morphs in polymorphic populations.[6,7,13,22,99] Why populations throughout the rest of the species range, which includes the Caribbean lowlands of Costa Rica and Nicaragua, remain uniformly red remains a more open question. A possible answer is that the beneficial effects of divergent coloration are transient and that rare morphs eventually go extinct in the larger populations on the mainland but may locally fix on islands or isolated populations (i.e., DB) with a smaller population size.

Fitness trade-offs between predation, female choice, and male-male competition likely shift over time, influenced by environmental changes. In BW and DB—both human-disturbed yet densely populated by *O. pumilio*—we find evidence of selection favoring new morphs. These trade-offs may periodically favor rare or common morphs, and with different morphs on neighboring islands acting as reservoirs of genetic variation, a dynamic system could emerge, maintaining the high color diversity seen in the Bocas del Toro archipelago. While our results do not directly confirm this, prior research on male-male competition[13,22] and predation,[28] along with our findings on selection for novel color morphs introduced by gene flow, support this hypothesis.

Another hypothesis to explain why color variation and polymorphism in *O. pumilio* appear to be limited to the Bocas del Toro area of Panama could be the existence of a locus affecting behavior, where an allele that affects the development of learned color-dependent male-male aggression and female choice is limited to the Bocas del Toro lineage.[6] In this case, the selection we observed favoring rare coloration should be limited to lineages that also bear such an "imprinting" allele. More behavioral studies in *O. pumilio*, both within and outside Bocas del Toro, will be needed to investigate this hypothesis. In either case, our results demonstrate that the polymorphisms in Bocas del Toro are driven by selection that, at least temporarily, favors rare morphs and cannot be explained simply as a consequence of drift associated with bottlenecks during colonization or island formation.

Our study has several limitations. One major challenge is the highly repetitive and large genome of *O. pumilio*. The currently available reference genome is highly fragmented, and a more complete assembly could help reduce some of the noise in our

results. Another limitation is our use of exome capture with low coverage. This approach was chosen to reduce costs while maximizing the number of populations and individuals sampled across different morphs ($n = 347$), making it a valuable resource for future research. However, exome capture limits our ability to genotype all positions, meaning we may have missed the exact causal variant responsible for these color polymorphisms. Regarding the GWAS, we acknowledge that using imputed phenotype values per morph rather than individual-level measurements reduces our ability to detect loci that cause phenotypic variation within morphs and may simplify the inferred genetic architecture. Nonetheless, evidence supports a more complex basis for coloration: multiple genes identified as PBS outliers correspond to known pigmentation pathways, and previous gene-expression studies[43,44] also implicate several color-related genes. Taken together, these results suggest that, while the full architecture likely involves multiple loci, the different GWAS performed here capture the strongest-effect variants that are most influential in differentiating color morphs.

For demographic modeling, our reliance on exome data precluded restricting analyses to putatively neutral regions when constructing the site frequency spectrum (SFS), which would be ideal for demographic inference. In addition, our model assumes a simple split with constant migration. More realistic scenarios involving temporally variable migration linked to past changes in land configuration and sea level would likely better reflect the history of these populations but would be difficult to optimize without substantial overparameterization. More broadly, demographic inference based on the SFS is inherently limited, as distinct demographic histories can produce similar genomic patterns.[49] In a geographically structured system such as *Oophaga pumilio*, which has experienced repeated isolation and reconnection, parameters related to population size changes and gene flow may therefore not be uniquely identifiable. Our inferred demographic histories should be interpreted in this context.

Despite these limitations, our study provides valuable insights into the evolutionary dynamics of color variation in *O. pumilio*. By integrating genomic data with phenotypic measurements—including color (spectrometric values), carotenoid content (HPLC), gene expression (RNA sequencing [RNA-seq] and qPCR), and pigment proportions—we offer a comprehensive framework for studying color evolution. Additionally, we propose key candidate genes and potential mechanisms underlying color variation, laying a strong foundation for future research. Improved genomic resources and demographic models will further enhance our understanding of the genetic and ecological factors shaping color diversity in this species. Moreover, our study demonstrates a cost-effective approach for investigating populations with highly repetitive, large genomes, making it a valuable model for similar systems.

Our findings highlight how uncovering the genetic basis of color variation in *Oophaga pumilio* provides a powerful window into the mechanisms of adaptation and diversification in natural populations. More broadly, understanding how specific genes shape striking phenotypic diversity in this system contributes to fundamental questions in evolutionary biology, including the predictability of adaptation, the role of selection in maintaining diversity, and the processes by which novel traits spread across populations.

RESOURCE AVAILABILITY

Lead contact

Requests for further information and resources should be directed to and will be fulfilled by the lead contact, Diana Aguilar-Gómez (dianaguilr@gmail.com).

Materials availability

This study did not generate any new, unique reagents.

Data and code availability

- The sequencing files are available at the NCBI BioProject database under accession NCBI: PRJNA760522 (*Oophaga pumilio* exomes from Bocas del Toro).
- The exome capture design can be accessed through Dryad (https://datadryad.org/dataset/doi:10.5061/dryad.np5hqc055).
- All code used in this study is available at https://github.com/aguilar-gomez/pumilioAnalysis.
- Any additional information required to reanalyze the data reported in this work paper is available from the lead contact upon request.

ACKNOWLEDGMENTS

We thank Adam Chois for help cropping frog pictures, Professor Lauren O'Connell for sharing the *Oophaga sylvatica* genome, Ariel Rodriguez for sharing the annotation from their *O. pumilio* genome, and Adam Stuckert for sharing the *Ranitomeya imitator* genome. This work was funded by the National Science Foundation (NSF DEB 1655336, Collaborative Research: Genomic and phenotypic analyses of color pattern divergence in a mimetic radiation of poison frogs). D.A.-G. was funded by Fulbright Garcia-Robles and UC MEXUS-CONACYT while working on this project.

AUTHOR CONTRIBUTIONS

Conceptualization, D.A.-G., C.L.R.-Z., and R.N.; methodology, D.A.-G., L.F., and T.L.; investigation, D.A.-G., L.F., L.Y., L.L.S., and A.G.; software, D.A.-G. and A.H.V.; formal analysis, D.A.-G., L.F., and L.Y.; data curation, D.A.-G. and E.S.; writing – original draft, D.A.-G. and R.N.; writing – review & editing, D.A.-G., L.Y., A.S., Y.Y., T.L., M.M., K.J.M., C.L.R.-Z., and R.N.; visualization, D.A.-G. and L.Y.; funding acquisition, D.A.-G. and R.N.; resources, L.F., A.S., Y.Y., M.M., K.J.M., C.L.R.-Z., and R.N.; supervision, D.A.-G., C.L.R.-Z., and R.N.

DECLARATION OF INTERESTS

The authors declare no competing interests.

STAR★METHODS

Detailed methods are provided in the online version of this paper and include the following:

- KEY RESOURCES TABLE
- EXPERIMENTAL MODEL AND STUDY PARTICIPANT DETAILS
- METHOD DETAILS
  - Reflectance Spectrometry and Color Assignment
  - Pigment Quantification
  - Carotenoid Composition
  - Probe Design for Exome Capture
  - Library prep
  - Pooling and Exome Capture
  - Sequencing and Read processing
  - Mapping and annotation
  - SNP filtering
  - Population Structure Analyses
  - Demographic Inference
  - Synteny alignment
  - Coding mutations and protein trees
  - Average genomic tree and gene trees

SUPPLEMENTAL INFORMATION

Supplemental information can be found online at https://doi.org/10.1016/j.cub.2026.01.041.

Received: September 25, 2024
Revised: September 5, 2025
Accepted: January 16, 2026

REFERENCES

1. Daly, J.W., and Myers, C.W. (1967). Toxicity of Panamanian poison frogs (Dendrobates): some biological and chemical aspects. Science *156*, 970–973. https://doi.org/10.1126/science.156.3777.970.
2. Coleman, J.L. (2023). Why the striking diversity of conspicuous color patterns in a poison frog from Central America? 58, 70–74.
3. Summers, K., Bermingham, E., Weigt, L., McCafferty, S., and Dahlstrom, L. (1997). Phenotypic and genetic divergence in three species of dart-poison frogs with contrasting parental behavior. J. Hered. *88*, 8–13. https://doi.org/10.1093/oxfordjournals.jhered.a023065.
4. Anderson, R.P., and Handley, C.O., Jr. (2002). Dwarfism in insular sloths: biogeography, selection, and evolutionary rate. Evolution *56*, 1045–1058. https://doi.org/10.1111/j.0014-3820.2002.tb01415.x.
5. Summers, K., Cronin, T.W., and Kennedy, T. (2003). Variation in spectral reflectance among populations of Dendrobates pumilio, the strawberry poison frog, in the Bocas del Toro Archipelago, Panama. J. Biogeogr. *30*, 35–53. https://doi.org/10.1046/j.1365-2699.2003.00795.x.
6. Yang, Y., Servedio, M.R., and Richards-Zawacki, C.L. (2019). Imprinting sets the stage for speciation. Nature *574*, 99–102. https://doi.org/10.1038/s41586-019-1599-z.
7. Dreher, C.E., Cummings, M.E., and Pröhl, H. (2015). An analysis of predator selection to affect aposematic coloration in a poison frog species. PLoS One *10*, e0130571. https://doi.org/10.1371/journal.pone.0130571.
8. Prates, I., Paz, A., Brown, J.L., and Carnaval, A.C. (2019). Effects of prey turnover on poison frog toxins: using landscape ecology approach to assess how biotic interactions affect species phenotypes. Preprint at bioRxiv. https://doi.org/10.1101/695171.
9. Dugas, M.B., Halbrook, S.R., Killius, A.M., del Sol, J.F., and Richards-Zawacki, C.L. (2015). Colour and escape behaviour in polymorphic populations of an aposematic poison frog. Ethology *121*, 813–822. https://doi.org/10.1111/eth.12396.
10. Rudh, A., Rogell, B., and Höglund, J. (2007). Non-gradual variation in colour morphs of the strawberry poison frog Dendrobates pumilio: genetic and geographical isolation suggest a role for selection in maintaining polymorphism. Mol. Ecol. *16*, 4284–4294. https://doi.org/10.1111/j.1365-294X.2007.03479.x.
11. Pröhl, H., and Hödl, W. (1999). Parental investment, potential reproductive rates, and mating system in the strawberry dart-poison frog, Dendrobates pumilio. Behav. Ecol. Sociobiol. *46*, 215–220. https://doi.org/10.1007/s002650050612.
12. Maan, M.E., and Cummings, M.E. (2012). Poison frog colors are honest signals of toxicity, particularly for bird predators. Am. Nat. *179*, E1–E14. https://doi.org/10.1086/663197.
13. Yang, Y., Dugas, M.B., Sudekum, H.J., Murphy, S.N., and Richards-Zawacki, C.L. (2018). Male-male aggression is unlikely to stabilize a poison frog polymorphism. J. Evol. Biol. *31*, 457–468. https://doi.org/10.1111/jeb.13243.
14. Richards-Zawacki, C.L., Wang, I.J., and Summers, K. (2012). Mate choice and the genetic basis for colour variation in a polymorphic dart frog: inferences from a wild pedigree. Mol. Ecol. *21*, 3879–3892. https://doi.org/10.1111/j.1365-294X.2012.05644.x.
15. Richards-Zawacki, C.L., and Cummings, M.E. (2011). Intraspecific reproductive character displacement in a polymorphic poison dart frog, Dendrobates pumilio. Evolution *65*, 259–267. https://doi.org/10.1111/j.1558-5646.2010.01124.x.
16. Dugas, M.B., and Richards-Zawacki, C.L. (2015). A captive breeding experiment reveals no evidence of reproductive isolation among lineages of a polytypic poison frog. Biol. J. Linn. Soc. *116*, 52–62. https://doi.org/10.1111/bij.12571.
17. Wang, I.J., and Summers, K. (2010). Genetic structure is correlated with phenotypic divergence rather than geographic isolation in the highly polymorphic strawberry poison-dart frog. Mol. Ecol. *19*, 447–458. https://doi.org/10.1111/j.1365-294X.2009.04465.x.
18. Ruxton, G.D., Allen, W.L., Sherratt, T.N., and Speed, M.P. (2019). Avoiding Attack: The Evolutionary Ecology of Crypsis, Aposematism, and Mimicry (Oxford University Press).
19. Noonan, B.P., and Comeault, A.A. (2009). The role of predator selection on polymorphic aposematic poison frogs. Biol. Lett. *5*, 51–54. https://doi.org/10.1098/rsbl.2008.0586.
20. Gehara, M., Summers, K., and Brown, J.L. (2013). Population expansion, isolation and selection: novel insights on the evolution of color diversity in the strawberry poison frog. Evol. Ecol. *27*, 797–824. https://doi.org/10.1007/s10682-013-9652-0.
21. Tazzyman, S.J., and Iwasa, Y. (2010). Sexual selection can increase the effect of random genetic drift—a quantitative genetic model of polymorphism in Oophaga pumilio, the strawberry poison-dart frog. Evolution *64*, 1719–1728. https://doi.org/10.1111/j.1558-5646.2009.00923.x.
22. Yang, Y., Blomenkamp, S., Dugas, M.B., Richards-Zawacki, C.L., and Pröhl, H. (2019). Mate choice versus mate preference: inferences about color-assortative mating differ between field and lab assays of poison frog behavior. Am. Nat. *193*, 598–607. https://doi.org/10.1086/702249.
23. González-Santoro, M., Sudekum, H.J., Murphy, S.N., Richards, R.P., Yang, Y., and Richards-Zawacki, C.L. (2025). Sexual selection's role in the persistence of polymorphism in an aposematic signal. Evolution *79*, 2643–2653. https://doi.org/10.1093/evolut/qpaf189.
24. Brown, J.L., Maan, M.E., Cummings, M.E., and Summers, K. (2010). Evidence for selection on coloration in a Panamanian poison frog: a coalescent-based approach. J. Biogeogr. *37*, 891–901. https://doi.org/10.1111/j.1365-2699.2009.02260.x.
25. Lehman, M.R., González-Santoro, M., and Richards-Zawacki, C.L. (2024). Little evidence for color- or size-based mating preferences by male strawberry poison frogs (Oophaga pumilio). Behav. Ecol. Sociobiol. *78*, 19. https://doi.org/10.1007/s00265-024-03436-9.
26. Summers, K., Symula, R., Clough, M., and Cronin, T. (1999). Visual mate choice in poison frogs. Proc. Biol. Sci. *266*, 2141–2145. https://doi.org/10.1098/rspb.1999.0900.
27. Reynolds, R.G., and Fitzpatrick, B.M. (2007). Assortative mating in poison-dart frogs based on an ecologically important trait. Evolution *61*, 2253–2259. https://doi.org/10.1111/j.1558-5646.2007.00174.x.
28. Hegna, R.H., Saporito, R.A., and Donnelly, M.A. (2013). Not all colors are equal: predation and color polytypism in the aposematic poison frog Oophaga pumilio. Evol. Ecol. *27*, 831–845. https://doi.org/10.1007/s10682-012-9605-z.
29. Jin, Y., Aguilar-Gómez, D., Y C Brandt, D., Square, T.A., Li, J., Liu, Z., Wang, T., Sudmant, P.H., Miller, C.T., and Nielsen, R. (2022). Population genomics of variegated toad-headed lizard Phrynocephalus versicolor

and its adaptation to the colorful sand of the Gobi Desert. Genome Biol. Evol. *14*, evac076. https://doi.org/10.1093/gbe/evac076.

30. Bagnara, J.T., Frost, S.K., and Matsumoto, J. (1978). On the development of pigment patterns in amphibians. Am. Zool. *18*, 301–312. https://doi.org/10.1093/icb/18.2.301.
31. Bagnara, J.T., Fernandez, P.J., and Fujii, R. (2007). On the blue coloration of vertebrates. Pigment Cell Res. *20*, 14–26. https://doi.org/10.1111/j.1600-0749.2006.00360.x.
32. Toomey, M.B., Marques, C.I., Araújo, P.M., Huang, D., Zhong, S., Liu, Y., Schreiner, G.D., Myers, C.A., Pereira, P., Afonso, S., et al. (2022). A mechanism for red coloration in vertebrates. Curr. Biol. *32*, 4201–4214.e12. https://doi.org/10.1016/j.cub.2022.08.013.
33. Kelsh, R.N. (2004). Genetics and evolution of pigment patterns in fish. Pigment Cell Res. *17*, 326–336. https://doi.org/10.1111/j.1600-0749.2004.00174.x.
34. Bagnara, J.T., Taylor, J.D., and Hadley, M.E. (1968). The dermal chromatophore unit. J. Cell Biol. *38*, 67–79. https://doi.org/10.1083/jcb.38.1.67.
35. Wang, I.J., and Shaffer, H.B. (2008). Rapid color evolution in an aposematic species: a phylogenetic analysis of color variation in the strikingly polymorphic strawberry poison-dart frog. Evolution *62*, 2742–2759. https://doi.org/10.1111/j.1558-5646.2008.00507.x.
36. Kinoshita, S., and Yoshioka, S. (2005). Structural colors in nature: the role of regularity and irregularity in the structure. ChemPhysChem *6*, 1442–1459. https://doi.org/10.1002/cphc.200500007.
37. Maoka, T. (2020). Carotenoids as natural functional pigments. J. Nat. Med. *74*, 1–16. https://doi.org/10.1007/s11418-019-01364-x.
38. Ogilvy, V., Preziosi, R.F., and Fidgett, A.L. (2012). A brighter future for frogs? The influence of carotenoids on the health, development and reproductive success of the red-eye tree frog. Anim. Conserv. *15*, 480–488. https://doi.org/10.1111/j.1469-1795.2012.00536.x.
39. Stückler, S., Cloer, S., Hödl, W., and Preininger, D. (2022). Carotenoid intake during early life mediates ontogenetic colour shifts and dynamic colour change during adulthood. Anim. Behav. *187*, 121–135. https://doi.org/10.1016/j.anbehav.2022.03.007.
40. Taboada, C., Brunetti, A.E., Lyra, M.L., Fitak, R.R., Faigón Soverna, A., Ron, S.R., Lagorio, M.G., Haddad, C.F.B., Lopes, N.P., Johnsen, S., et al. (2020). Multiple origins of green coloration in frogs mediated by a novel biliverdin-binding serpin. Proc. Natl. Acad. Sci. USA *117*, 18574–18581. https://doi.org/10.1073/pnas.2006771117.
41. Silverstone, P.A. (1976). A Revision of the Poison-Arrow Frogs of the Genus Phyllobates Bibron in Sagra (Family Dendrobatidae) (Natural History Museum of Los Angeles County).
42. Hauswaldt, J.S., Ludewig, A.-K., Vences, M., and Pröhl, H. (2011). Widespread co-occurrence of divergent mitochondrial haplotype lineages in a Central American species of poison frog (Oophaga pumilio). J. Biogeogr. *38*, 711–726. https://doi.org/10.1111/j.1365-2699.2010.02438.x.
43. Rodríguez, A., Mundy, N.I., Ibáñez, R., and Pröhl, H. (2020). Being red, blue and green: the genetic basis of coloration differences in the strawberry poison frog (Oophaga pumilio). BMC Genomics *21*, 301. https://doi.org/10.1186/s12864-020-6719-5.
44. Stuckert, A.M.M., Freeborn, L., Howell, K.A., Yang, Y., Nielsen, R., Richards-Zawacki, C., and MacManes, M.D. (2023). Transcriptomic analyses during development reveal mechanisms of integument structuring and color production. Evol. Ecol. *38*, 657–678. https://doi.org/10.1007/s10682-023-10256-2.
45. Freeborn, L.R. (2020). The Genetic, Cellular, and Evolutionary Basis of Skin Coloration in the Highly Polymorphic Poison Frog, Oophaga pumilio.
46. Rogers, R.L., Zhou, L., Chu, C., Márquez, R., Corl, A., Linderoth, T., Freeborn, L., MacManes, M.D., Xiong, Z., Zheng, J., et al. (2018). Genomic takeover by transposable elements in the strawberry poison frog. Mol. Biol. Evol. *35*, 2913–2927. https://doi.org/10.1093/molbev/msy185.
47. Cheng, J.Y., Mailund, T., and Nielsen, R. (2017). Fast admixture analysis and population tree estimation for SNP and NGS data. Bioinformatics *33*, 2148–2155. https://doi.org/10.1093/bioinformatics/btx098.
48. Nielsen, S.V., Vaughn, A.H., Leppälä, K., Landis, M.J., Mailund, T., and Nielsen, R. (2023). Bayesian inference of admixture graphs on Native American and Arctic populations. PLoS Genet. *19*, e1010410. https://doi.org/10.1371/journal.pgen.1010410.
49. Gutenkunst, R., Hernandez, R., Williamson, S., and Bustamante, C. (2010). Diffusion approximations for demographic inference: DaDi. Nat. Prec. https://doi.org/10.1038/npre.2010.4594.1.
50. Crawford, A.J. (2003). Relative rates of nucleotide substitution in frogs. J. Mol. Evol. *57*, 636–641. https://doi.org/10.1007/s00239-003-2513-7.
51. Santos, J.C. (2012). Fast molecular evolution associated with high active metabolic rates in poison frogs. Mol. Biol. Evol. *29*, 2001–2018. https://doi.org/10.1093/molbev/mss069.
52. Oksanen, J., Simpson, G.L., Blanchet, F.G., Kindt, R., Legendre, P., Minchin, P.R., O'Hara, R.B., Solymos, P., Stevens, M.H.H., Szoecs, E., et al. (2025). vegan: Community Ecology Package. https://cran.r-project.org/web/packages/vegan/vegan.pdf.
53. Dessinioti, C., Stratigos, A.J., Rigopoulos, D., and Katsambas, A.D. (2009). A review of genetic disorders of hypopigmentation: lessons learned from the biology of melanocytes. Exp. Dermatol. *18*, 741–749. https://doi.org/10.1111/j.1600-0625.2009.00896.x.
54. Anderson, H., Salonen, M., Toivola, S., Blades, M., Lyons, L.A., Forman, O.P., Hytönen, M.K., and Lohi, H. (2024). A new Finnish flavor of feline coat coloration, "salmiak," is associated with a 95-kb deletion downstream of the KIT gene. Anim. Genet. *55*, 676–680. https://doi.org/10.1111/age.13438.
55. Miller, C.T., Beleza, S., Pollen, A.A., Schluter, D., Kittles, R.A., Shriver, M.D., and Kingsley, D.M. (2007). cis-Regulatory changes in Kit ligand expression and parallel evolution of pigmentation in sticklebacks and humans. Cell *131*, 1179–1189. https://doi.org/10.1016/j.cell.2007.10.055.
56. Dodge, T.O., Kim, B.Y., Baczenas, J.J., Banerjee, S.M., Gunn, T.R., Donny, A.E., Given, L.A., Rice, A.R., Haase Cox, S.K., Weinstein, M.L., et al. (2024). Structural genomic variation and behavioral interactions underpin a balanced sexual mimicry polymorphism. Curr. Biol. *34*, 4662–4676.e9. https://doi.org/10.1016/j.cub.2024.08.053.
57. Stryjewski, K.F., and Sorenson, M.D. (2017). Mosaic genome evolution in a recent and rapid avian radiation. Nat. Ecol. Evol. *1*, 1912–1922. https://doi.org/10.1038/s41559-017-0364-7.
58. Kwon, Y.M., Vranken, N., Hoge, C., Lichak, M.R., Norovich, A.L., Francis, K.X., Camacho-Garcia, J., Bista, I., Wood, J., McCarthy, S., et al. (2022). Genomic consequences of domestication of the Siamese fighting fish. Sci. Adv. *8*, eabm4950. https://doi.org/10.1126/sciadv.abm4950.
59. Hultman, K.A., Bahary, N., Zon, L.I., and Johnson, S.L. (2007). Gene duplication of the zebrafish kit ligand and partitioning of melanocyte development functions to kit ligand a. PLoS Genet. *3*, e17. https://doi.org/10.1371/journal.pgen.0030017.
60. Waterhouse, A., Bertoni, M., Bienert, S., Studer, G., Tauriello, G., Gumienny, R., Heer, F.T., de Beer, T.A.P., Rempfer, C., Bordoli, L., et al. (2018). SWISS-MODEL: homology modelling of protein structures and complexes. Nucleic Acids Res. *46*, W296–W303. https://doi.org/10.1093/nar/gky427.
61. Rohrlich, S.T., and Porter, K.R. (1972). Fine structural observations relating to the production of color by the iridophores of a lizard. Anolis carolinensis. J. Cell Biol. *53*, 38–52. https://doi.org/10.1083/jcb.53.1.38.
62. Smyth, I.M., Wilming, L., Lee, A.W., Taylor, M.S., Gautier, P., Barlow, K., Wallis, J., Martin, S., Glithero, R., Phillimore, B., et al. (2006). Genomic anatomy of the Tyrp1 (brown) deletion complex. Proc. Natl. Acad. Sci. USA *103*, 3704–3709. https://doi.org/10.1073/pnas.0600199103.
63. Fang, W., Huang, J., Li, S., and Lu, J. (2022). Identification of pigment genes (melanin, carotenoid and pteridine) associated with skin color variant in red tilapia using transcriptome analysis. Aquaculture *547*, 737429. https://doi.org/10.1016/j.aquaculture.2021.737429.

64. Hooper, D.M., Griffith, S.C., and Price, T.D. (2019). Sex chromosome inversions enforce reproductive isolation across an avian hybrid zone. Mol. Ecol. *28*, 1246–1262. https://doi.org/10.1111/mec.14874.

65. Ahi, E.P., Lecaudey, L.A., Ziegelbecker, A., Steiner, O., Glabonjat, R., Goessler, W., Hois, V., Wagner, C., Lass, A., and Sefc, K.M. (2020). Comparative transcriptomics reveals candidate carotenoid color genes in an East African cichlid fish. BMC Genomics *21*, 54. https://doi.org/10.1186/s12864-020-6473-8.

66. McKinnon, J.S., Newsome, W.B., and Balakrishnan, C.N. (2022). Gene expression in male and female stickleback from populations with convergent and divergent throat coloration. Ecol. Evol. *12*, e8860. https://doi.org/10.1002/ece3.8860.

67. Stuckert, A.M.M., Chouteau, M., McClure, M., LaPolice, T.M., Linderoth, T., Nielsen, R., Summers, K., and MacManes, M.D. (2021). The genomics of mimicry: Gene expression throughout development provides insights into convergent and divergent phenotypes in a Müllerian mimicry system. Mol Ecol. *33*, e17345. https://doi.org/10.1111/mec.17345.

68. Hooper, D.M., McDiarmid, C.S., Powers, M.J., Justyn, N.M., Kučka, M., Hart, N.S., Hill, G.E., Andolfatto, P., Chan, Y.F., and Griffith, S.C. (2024). Spread of yellow-bill-color alleles favored by selection in the long-tailed finch hybrid system. Curr. Biol. *34*, 5444–5456.e8. https://doi.org/10.1016/j.cub.2024.10.019.

69. Moest, M., Van Belleghem, S.M., James, J.E., Salazar, C., Martin, S.H., Barker, S.L., Moreira, G.R.P., Mérot, C., Joron, M., Nadeau, N.J., et al. (2020). Selective sweeps on novel and introgressed variation shape mimicry loci in a butterfly adaptive radiation. PLoS Biol. *18*, e3000597. https://doi.org/10.1371/journal.pbio.3000597.

70. Setter, D., Mousset, S., Cheng, X., Nielsen, R., DeGiorgio, M., and Hermisson, J. (2020). VolcanoFinder: Genomic scans for adaptive introgression. PLoS Genet. *16*, e1008867. https://doi.org/10.1371/journal.pgen.1008867.

71. Clemons, M.R., Dimico, R.H., Black, C., Schlussler, M.K., Camerino, M.J., Aldinger-Gibson, K., Bartle, A., Reynolds, N., Eisenbrandt, D., Rogers, A., et al. (2023). The rod synapse in aging wildtype and Dscaml1 mutant mice. PLoS One *18*, e0290257. https://doi.org/10.1371/journal.pone.0290257.

72. Walkowski, W.G., Richards-Zawacki, C.L., Gordon, W.C., Bazan, N.G., and Farris, H.E. (2024). The relationship between spectral signals and retinal sensitivity in dendrobatid frogs. PLoS One *19*, e0312578. https://doi.org/10.1371/journal.pone.0312578.

73. von Lintig, J., and Vogt, K. (2000). Filling the gap in vitamin A research: molecular identification of an enzyme cleaving β-carotene to retinal *. J. Biol. Chem. *275*, 11915–11920. https://doi.org/10.1074/jbc.275.16.11915.

74. Kloer, D.P., and Schulz, G.E. (2006). Structural and biological aspects of carotenoid cleavage. Cell. Mol. Life Sci. *63*, 2291–2303. https://doi.org/10.1007/s00018-006-6176-6.

75. Enbody, E.D., Sprehn, C.G., Abzhanov, A., Bi, H., Dobreva, M.P., Osborne, O.G., Rubin, C.-J., Grant, P.R., Grant, B.R., and Andersson, L. (2021). A multispecies BCO2 beak color polymorphism in the Darwin's finch radiation. Curr. Biol. *31*, 5597–5604.e7. https://doi.org/10.1016/j.cub.2021.09.085.

76. Lim, H.C., Bennett, K.F.P., Justyn, N.M., Powers, M.J., Long, K.M., Kingston, S.E., Lindsay, W.R., Pease, J.B., Fuxjager, M.J., Bolton, P.E., et al. (2024). Sequential introgression of a carotenoid processing gene underlies sexual ornament diversity in a genus of manakins. Sci. Adv. *10*, eadn8339. https://doi.org/10.1126/sciadv.adn8339.

77. Toews, D.P.L., Taylor, S.A., Vallender, R., Brelsford, A., Butcher, B.G., Messer, P.W., and Lovette, I.J. (2016). Plumage genes and little else distinguish the genomes of hybridizing warblers. Curr. Biol. *26*, 2313–2318. https://doi.org/10.1016/j.cub.2016.06.034.

78. Baiz, M.D., Wood, A.W., Brelsford, A., Lovette, I.J., and Toews, D.P.L. (2021). Pigmentation genes show evidence of repeated divergence and multiple bouts of introgression in Setophaga warblers. Curr. Biol. *31*, 643–649.e3. https://doi.org/10.1016/j.cub.2020.10.094.

79. Cortés, R., Navarro, S., Agulleiro, M.J., Guillot, R., García-Herranz, V., Sánchez, E., and Cerdá-Reverter, J.M. (2014). Evolution of the melanocortin system. Gen. Comp. Endocrinol. *209*, 3–10. https://doi.org/10.1016/j.ygcen.2014.04.005.

80. Kobayashi, Y., Tsuchiya, K., Yamanome, T., Schiöth, H.B., and Takahashi, A. (2010). Differential expressions of melanocortin receptor subtypes in melanophores and xanthophores of barfin flounder. Gen. Comp. Endocrinol. *168*, 133–142. https://doi.org/10.1016/j.ygcen.2010.04.017.

81. Mizusawa, K., Yamamura, Y., Kasagi, S., Cerdá-Reverter, J.M., and Takahashi, A. (2018). Expression of genes for melanotropic peptides and their receptors for morphological color change in goldfish Carassius auratus. Gen. Comp. Endocrinol. *264*, 138–150. https://doi.org/10.1016/j.ygcen.2017.06.012.

82. Han, J., Hong, W.S., Wang, Q., Zhang, T.T., and Chen, S.X. (2019). The regulation of melanocyte-stimulating hormone on the pigment granule dispersion in the xanthophores and melanophores of the large yellow croaker (Larimichthys crocea). Aquaculture *507*, 7–20. https://doi.org/10.1016/j.aquaculture.2019.03.074.

83. Kobayashi, Y., Mizusawa, K., Chiba, H., Tagawa, M., and Takahashi, A. (2012). Further evidence on acetylation-induced inhibition of the pigment-dispersing activity of α-melanocyte-stimulating hormone. Gen. Comp. Endocrinol. *176*, 9–17. https://doi.org/10.1016/j.ygcen.2011.12.001.

84. Braasch, I., Brunet, F., Volff, J.-N., and Schartl, M. (2009). Pigmentation pathway evolution after whole-genome duplication in fish. Genome Biol. Evol. *1*, 479–493. https://doi.org/10.1093/gbe/evp050.

85. Samaniego Castruita, J.A., Westbury, M.V., and Lorenzen, E.D. (2020). Analyses of key genes involved in Arctic adaptation in polar bears suggest selection on both standing variation and de novo mutations played an important role. BMC Genomics *21*, 543. https://doi.org/10.1186/s12864-020-06940-0.

86. Toomey, M.B., Lopes, R.J., Araújo, P.M., Johnson, J.D., Gazda, M.A., Afonso, S., Mota, P.G., Koch, R.E., Hill, G.E., Corbo, J.C., et al. (2017). High-density lipoprotein receptor SCARB1 is required for carotenoid coloration in birds. Proc. Natl. Acad. Sci. USA *114*, 5219–5224. https://doi.org/10.1073/pnas.1700751114.

87. Yang, Z., Bai, C., Pu, Y., Kong, Q., Guo, Y., , et al.; Ouzhuluobu, Gengdeng, Liu, X., Zhao, Q., Qiu, Z. (2022). Genetic adaptation of skin pigmentation in highland Tibetans. Proc. Natl. Acad. Sci. USA *119*, e2200421119. https://doi.org/10.1073/pnas.2200421119.

88. Liu, S., Lorenzen, E.D., Fumagalli, M., Li, B., Harris, K., Xiong, Z., Zhou, L., Korneliussen, T.S., Somel, M., Babbitt, C., et al. (2014). Population genomics reveal recent speciation and rapid evolutionary adaptation in polar bears. Cell *157*, 785–794. https://doi.org/10.1016/j.cell.2014.03.054.

89. Kunieda, T., Nakagiri, M., Takami, M., Ide, H., and Ogawa, H. (1999). Cloning of bovine LYST gene and identification of a missense mutation associated with Chediak-Higashi syndrome of cattle. Mamm. Genome *10*, 1146–1149. https://doi.org/10.1007/s003359901181.

90. Anistoroaei, R., Krogh, A.K., and Christensen, K. (2013). A frameshift mutation in the LYSTgene is responsible for the Aleutian color and the associated Chédiak-Higashi syndrome in American mink. Anim. Genet. *44*, 178–183. https://doi.org/10.1111/j.1365-2052.2012.02391.x.

91. Ullate-Agote, A., Burgelin, I., Debry, A., Langrez, C., Montange, F., Peraldi, R., Daraspe, J., Kaessmann, H., Milinkovitch, M.C., and Tzika, A.C. (2020). Genome mapping of a LYST mutation in corn snakes indicates that vertebrate chromatophore vesicles are lysosome-related organelles. Proc. Natl. Acad. Sci. USA *117*, 26307–26317. https://doi.org/10.1073/pnas.2003724117.

92. Tharmarajah, G.T. (2015). The role of Adamts9 in melanoblast migration and modification of the skin proteome. PhD thesis (University of British Columbia). https://doi.org/10.14288/1.0166255.

93. McLean, C.A., Lutz, A., Rankin, K.J., Stuart-Fox, D., and Moussalli, A. (2017). Revealing the biochemical and genetic basis of color variation

in a polymorphic lizard. Mol. Biol. Evol. *34*, 1924–1935. https://doi.org/10.1093/molbev/msx136.

94. Kelsh, R.N., Harris, M.L., Colanesi, S., and Erickson, C.A. (2009). Stripes and belly-spots – a review of pigment cell morphogenesis in vertebrates. Semin. Cell Dev. Biol. *20*, 90–104. https://doi.org/10.1016/j.semcdb.2008.10.001.

95. Landrum, M.J., Lee, J.M., Riley, G.R., Jang, W., Rubinstein, W.S., Church, D.M., and Maglott, D.R. (2014). ClinVar: public archive of relationships among sequence variation and human phenotype. Nucleic Acids Res. *42*, D980–D985. https://doi.org/10.1093/nar/gkt1113.

96. Yuzawa, S., Opatowsky, Y., Zhang, Z., Mandiyan, V., Lax, I., and Schlessinger, J. (2007). Structural basis for activation of the receptor tyrosine kinase KIT by stem cell factor. Cell *130*, 323–334. https://doi.org/10.1016/j.cell.2007.05.055.

97. Papadopoulou, A., and Knowles, L.L. (2015). Genomic tests of the species-pump hypothesis: recent island connectivity cycles drive population divergence but not speciation in Caribbean crickets across the Virgin Islands. Evolution *69*, 1501–1517. https://doi.org/10.1111/evo.12667.

98. Coates, A.G., McNeill, D.F., Aubry, M.-P., Berggren, W.A., and Collins, L.S. (2005). An introduction to the geology of the Bocas del Toro Archipelago, Panama. Caribb. Caribb. J. Sci. *41*, 374–391.

99. Galeano, S.P., and Harms, K.E. (2016). Coloration in the polymorphic frog Oophaga pumilio associates with level of aggressiveness in intraspecific and interspecific behavioral interactions. Behav. Ecol. Sociobiol. *70*, 83–97. https://doi.org/10.1007/s00265-015-2027-5.

100. Maia, R., Gruson, H., Endler, J.A., and White, T.E. (2019). pavo 2: New tools for the spectral and spatial analysis of colour in r. Methods Ecol. Evol. *10*, 1097–1107. https://doi.org/10.1111/2041-210X.13174.

101. Warnes, G.R., Bolker, B., Bonebakker, L., Gentleman, R., Huber, W., Liaw, A., Lumley, T., Maechler, M., Magnusson, A., Moeller, S., et al. (2024). gplots: Various R Programming Tools for Plotting Data. https://cran.r-project.org/web/packages/gplots/index.html.

102. Dobin, A., Davis, C.A., Schlesinger, F., Drenkow, J., Zaleski, C., Jha, S., Batut, P., Chaisson, M., and Gingeras, T.R. (2013). STAR: ultrafast universal RNA-seq aligner. Bioinformatics *29*, 15–21. https://doi.org/10.1093/bioinformatics/bts635.

103. Bolger, A.M., Lohse, M., and Usadel, B. (2014). Trimmomatic: a flexible trimmer for Illumina sequence data. Bioinformatics *30*, 2114–2120. https://doi.org/10.1093/bioinformatics/btu170.

104. Li, H. (2013). Aligning sequence reads, clone sequences and assembly contigs with BWA-MEM. Preprint at arXiv. https://doi.org/10.48550/arXiv.1303.3997.

105. Danecek, P., Bonfield, J.K., Liddle, J., Marshall, J., Ohan, V., Pollard, M.O., Whitwham, A., Keane, T., McCarthy, S.A., Davies, R.M., et al. (2021). Twelve years of SAMtools and BCFtools. GigaScience *10*, giab008. https://doi.org/10.1093/gigascience/giab008.

106. Pertea, G., and Pertea, M. (2020). GFF utilities: GffRead and GffCompare. F1000Res 9, 304.

107. Korneliussen, T.S., Albrechtsen, A., and Nielsen, R. (2014). ANGSD: analysis of next generation sequencing data. BMC Bioinform. *15*, 356. https://doi.org/10.1186/s12859-014-0356-4.

108. Pickrell, J.K., and Pritchard, J.K. (2012). Inference of population splits and mixtures from genome-wide allele frequency data. PLoS Genet. *8*, e1002967. https://doi.org/10.1371/journal.pgen.1002967.

109. Baumdicker, F., Bisschop, G., Goldstein, D., Gower, G., Ragsdale, A.P., Tsambos, G., Zhu, S., Eldon, B., Ellerman, E.C., Galloway, J.G., et al. (2022). Efficient ancestry and mutation simulation with msprime 1.0. Genetics *220*, iyab229. https://doi.org/10.1093/genetics/iyab229.

110. Marçais, G., Delcher, A.L., Phillippy, A.M., Coston, R., Salzberg, S.L., and Zimin, A. (2018). MUMmer4: A fast and versatile genome alignment system. PLoS Comput. Biol. *14*, e1005944. https://doi.org/10.1371/journal.pcbi.1005944.

111. Zhou, X., and Stephens, M. (2012). Genome-wide efficient mixed-model analysis for association studies. Nat. Genet. *44*, 821–824. https://doi.org/10.1038/ng.2310.

112. Haas, B.J. (2023). TransDecoder: TransDecoder source (Github). https://github.com/TransDecoder/TransDecoder.

113. Love, M.I., Huber, W., and Anders, S. (2014). Moderated estimation of fold change and dispersion for RNA-seq data with DESeq2. Genome Biol. *15*, 550. https://doi.org/10.1186/s13059-014-0550-8.

114. Waterhouse, A.M., Procter, J.B., Martin, D.M.A., Clamp, M., and Barton, G.J. (2009). Jalview version 2—a multiple sequence alignment editor and analysis workbench. Bioinformatics *25*, 1189–1191. https://doi.org/10.1093/bioinformatics/btp033.

115. Vieira, F.G., Lassalle, F., Korneliussen, T.S., and Fumagalli, M. (2015). Improving the estimation of genetic distances from next-generation sequencing data. Biol. J. Linn. Soc. *117*, 139–149. https://doi.org/10.1111/bij.12511.

116. Lefort, V., Desper, R., and Gascuel, O. (2015). FastME 2.0: a comprehensive, accurate, and fast distance-based phylogeny inference program. Mol. Biol. Evol. *32*, 2798–2800. https://doi.org/10.1093/molbev/msv150.

117. Siddiqi, A., Cronin, T.W., Loew, E.R., Vorobyev, M., and Summers, K. (2004). Interspecific and intraspecific views of color signals in the strawberry poison frog Dendrobates pumilio. J. Exp. Biol. *207*, 2471–2485. https://doi.org/10.1242/jeb.01047.

118. Schneider, C.A., Rasband, W.S., and Eliceiri, K.W. (2012). NIH Image to ImageJ: 25 years of image analysis. Nat. Methods *9*, 671–675. https://doi.org/10.1038/nmeth.2089.

119. Egozcue, J.J., Pawlowsky-Glahn, V., Mateu-Figueras, G., and Barceló-Vidal, C. (2003). Isometric logratio transformations for compositional data analysis. Math. Geol. *35*, 279–300. https://doi.org/10.1023/A:1023818214614.

120. McGraw, K.J. (2006). Mechanics of carotenoid-based colouration. In Bird Coloration, volume 1: Mechanisms and measurements, G.E. Hill, and K.J. McGraw, eds. (Harvard University Press).

121. Crothers, L., Saporito, R.A., Yeager, J., Lynch, K., Friesen, C., Richards-Zawacki, C.L., McGraw, K., and Cummings, M. (2016). Warning signal properties covary with toxicity but not testosterone or aggregate carotenoids in a poison frog. Evol. Ecol. *30*, 601–621. https://doi.org/10.1007/s10682-016-9830-y.

122. Jolivet, P., and Joseph. (2020). SPRI bead mix v1 (ZappyLab, Inc.). https://doi.org/10.17504/protocols.io.bnz4mf8w.

123. Benham, P.M., Cicero, C., Davila, M.M., Enbody, E.D., Miller, K.S., Shultz, A.J., Smith, L.L., Nachman, M.W., and Bowie, R.C.K. (2025). Patterns of genetic diversity within three California quail species are best explained by climate and landscape changes. Mol. Ecol. *34*, e70093. https://doi.org/10.1111/mec.70093.

124. NCBI Resource Coordinators (2018). Database resources of the National Center for Biotechnology Information. Nucleic Acids Res. *46*, D8–D13. https://doi.org/10.1093/nar/gkx1095.

125. Meisner, J., and Albrechtsen, A. (2018). Inferring population structure and admixture proportions in low-depth NGS data. Genetics *210*, 719–731. https://doi.org/10.1534/genetics.118.301336.

126. Pfaffl, M.W. (2001). A new mathematical model for relative quantification in real-time RT-PCR. Nucleic Acids Res. *29*, e45. https://doi.org/10.1093/nar/29.9.e45.

127. Fumagalli, M., Vieira, F.G., Linderoth, T., and Nielsen, R. (2014). ngsTools: methods for population genetics analyses from next-generation sequencing data. Bioinformatics *30*, 1486–1487. https://doi.org/10.1093/bioinformatics/btu041.

128. Hanghøj, K., Moltke, I., Andersen, P.A., Manica, A., and Korneliussen, T.S. (2019). Fast and accurate relatedness estimation from high-throughput sequencing data in the presence of inbreeding. GigaScience *8*, giz034. https://doi.org/10.1093/gigascience/giz034.

129. Zhou, X., Carbonetto, P., and Stephens, M. (2013). Polygenic modeling with bayesian sparse linear mixed models. PLoS Genet. *9*, e1003264. https://doi.org/10.1371/journal.pgen.1003264.

130. Camacho, C., Coulouris, G., Avagyan, V., Ma, N., Papadopoulos, J., Bealer, K., and Madden, T.L. (2009). BLAST+: architecture and applications. BMC Bioinform. *10*, 421. https://doi.org/10.1186/1471-2105-10-421.

131. Hudson, R.R., Kreitman, M., and Aguadé, M. (1987). A test of neutral molecular evolution based on nucleotide data. Genetics *116*, 153–159. https://doi.org/10.1093/genetics/116.1.153.

132. Kim, S.Y., Lohmueller, K.E., Albrechtsen, A., Li, Y., Korneliussen, T., Tian, G., Grarup, N., Jiang, T., Andersen, G., Witte, D., et al. (2011). Estimation of allele frequency and association mapping using next-generation sequencing data. BMC Bioinform. *12*, 231. https://doi.org/10.1186/1471-2105-12-231.

133. Korneliussen, T.S., Moltke, I., Albrechtsen, A., and Nielsen, R. (2013). Calculation of Tajima's D and other neutrality test statistics from low depth next-generation sequencing data. BMC Bioinform. *14*, 289. https://doi.org/10.1186/1471-2105-14-289.

134. Tajima, F. (1989). Statistical method for testing the neutral mutation hypothesis by DNA polymorphism. Genetics *123*, 585–595. https://doi.org/10.1093/genetics/123.3.585.

Please cite this article in press as: Aguilar-Gómez et al., Selection-driven color variation in the aposematic strawberry poison frog, *Oophaga pumilio*, Current Biology (2026), https://doi.org/10.1016/j.cub.2026.01.041

STAR★METHODS

KEY RESOURCES TABLE

REAGENT or RESOURCE	SOURCE	IDENTIFIER
Biological samples		
Strawberry poison frog (*Oophaga pumilio*)	This paper	N/A
Deposited data		
Strawberry poison frog exome sequencing data in fastq format	This paper	BioProject SRA: PRJNA760522
Exome capture design for the strawberry poison frog, *Oophaga pumilio*, in Bocas del Toro	This paper	Dryad: https://doi.org/10.5061/dryad.np5hqc055
Re-scaffolded genome and supertranscriptome of the strawberry poison frog (*Oophaga pumilio*)	Rodriguez et al.[43]	https://zenodo.org/records/3696842
Little devil poison frog (*Oophaga sylvatica*) reference genome	Lauren O' Connell	BioProject SRA: PRJNA909817
Oligonucleotides		
qPCR *psip1* forward primer: CTCCATAGATGCCAGGCTTCA	This paper	N/A
qPCR *psip1* reverse primer: CATGCTGCATGGTGACCTG	This paper	N/A
qPCR *ttc39b* forward primer: CCATCTCGGTTATGCAGGCT	This paper	N/A
qPCR *ttc39b* reverse primer: GGTCTCCAGTCTGTTTGGACA	This paper	N/A
qPCR *sdha* forward primer: GGCTCTGATTGGTTGGGTGA	This paper	N/A
qPCR*sdha* reverse primer: ACTTCAAGCTTTGCCCTCCA	This paper	N/A
Software and algorithms		
pavo R package	Maia et al.[100]	https://cran.r-project.org/web/packages/pavo/
gplots R package	Warnes et al.[101]	https://cran.r-project.org/web/packages/gplots/
STAR 2.7	Dobin et al.[102]	https://github.com/alexdobin/STAR
Trimmomatic-0.39	Bolger et al.[103]	https://github.com/usadellab/Trimmomatic/releases/tag/v0.39
BWA-MEM version 0.7.17	Li[104]	https://github.com/lh3/bwa
SAMtools 1.11	Danecek et al.[105]	https://github.com/samtools/samtools
BCFtools version 1.15.1	Danecek et al.[105]	https://github.com/samtools/bcftools
GffRead	Pertea and Perteav[106]	https://github.com/gpertea/gffread
ANGSD version 0.941	Korneliussen et al.[107]	https://github.com/ANGSD/angsd
OHANA	Cheng et al.[47]	https://github.com/jade-cheng/ohana
TreeMix	Pickrell and Pritchard[108]	https://bitbucket.org/nygcresearch/treemix
AdmixtureBayes	Nielsen et al.[48]	https://github.com/avaughn271/AdmixtureBayes
msprime	Baumdicker et al.[109]	https://tskit.dev/software/msprime.html
dadi	Gutenkunst et al.[49]	https://dadi.readthedocs.io/en/latest/
MUMmer4	Marçais et al.[110]	https://github.com/mummer4/mummer
GEMMA 0.98.5	Zhou and Stephens[111]	https://github.com/genetics-statistics/GEMMA
TransDecoder	Haas[112]	https://github.com/sghignone/TransDecoder
DESeq2	Love et al.[113]	https://bioconductor.org/packages/release/bioc/html/DESeq2.html
SWISS-MODEL	Waterhouse et al.[60]	https://swissmodel.expasy.org/
Jalview	Waterhouse et al.[114]	https://www.jalview.org/

(*Continued on next page*)

Continued

REAGENT or RESOURCE	SOURCE	IDENTIFIER
ngsDist	Vieiria et al.[115]	https://github.com/fgvieira/ngsDist
FASTME 2.1.6.2	Lefort et al.[116]	https://gite.lirmm.fr/atgc/FastME
ngsRelate version 2	Hanghøj et al.[12]	https://github.com/ANGSD/NgsRelate
Exome capture processing pipeline	Computational Genomics Resource Laboratory at UC Berkeley	https://github.com/CGRL-QB3-UCBerkeley/MarkerDevelopmentPopGen
Site windows of Tajima's D and nucleotide diversity	This paper	https://github.com/aguilar-gomez/angsdSupplement/
Analysis pipeline and custom scripts	This paper	https://github.com/aguilar-gomez/pumilioAnalysis

EXPERIMENTAL MODEL AND STUDY PARTICIPANT DETAILS

A total of 347 *Oophaga pumilio* frogs were sampled from the Bocas Del Toro Province in Panama. Sampling was conducted under approval from the University of Pittsburgh IACUC (protocol no. 15106566) and permits issued by the Panamanian government (Mi-Ambiente, Collection/research permit no. SC/A-42-16 and export permit no. SEX/A-122-16). Aguacate blue morph frogs were sampled from the Aguacate Peninsula ([AG] n=37: Shark Hole n=30 [SK] and Rana Azul n=7l [RA]), which is still part of the mainland but located a short distance from the archipelago. From the same peninsula, we sampled frogs from the blue-red transition zone Dolphin Bay ([DB] n: red=31, blue=32 and intermediate=41). The orange frogs were sampled from Solarte ([HP] n=30, Hospital Point). We sampled frogs from the San Cristobal morph, which is red with blue legs and sometimes black speckles ([SC] n=26, San Cristobal and South San Cristobal). Popa green frogs were sampled from two locations on Popa Island ([PP] n=37, Punta Laurel [PO] and Popa Dos [PD]). Red frogs were sampled from Bastimentos island in Tranquilo Bay ([TB] n = 35). At the northwestern tip of this same island, we sampled a polymorphic population known as Bastimentos West (BW). We sampled yellow frogs (BW-Y, n=30) and red frogs (BW-R, n=33) from this area. We also collected green frogs from two locations on Colon Island ([CL] n=15, Boca del Drago and La Gruta). The exact locations are omitted because of the persisting illegal pet trade of *O. pumilio*. Frogs were sampled from distinct local "neighborhoods" to minimize the probability of collecting closely related individuals.

METHOD DETAILS

Reflectance Spectrometry and Color Assignment

Color measurements were based on the average of five representative individuals for each population. More details of these samples and the complete detailed methods can be found in Freeborn.[45] The values measured from Freeborn[45] were imputed to the samples from this study, assigning the average value of its corresponding population (and specific morph in the Dolphin Bay and Bastimentos West polymorphic populations). Dorsal coloration of each animal was measured at three predefined regions per side with a JAZA1507 reflectance spectrophotometer connected to Oceanview software. Measurements were taken in a darkroom and the instrument was calibrated at each session's start with light and dark standards. Upon completing one round of measurements for a set of five frogs, sample order was randomized and the process was repeated a second time for each frog. Using pavo[100] in R, raw spectral data were processed to visualize spectra and calculate colorimetric variables. Spectra were restricted to the UV-visible range, 300-700nm, and wavelengths were averaged into 1nm bins. We used the summary.rspec function in pavo to calculate total brightness (B1), the wavelength at the reflectance midpoint (hue, H3), and the relative contribution of a spectral range to total brightness (chroma, S1). Pavo splits S1 into six wavelength ranges corresponding with trichromat-perceived hues: S_U (ultraviolet, lambda min-400nm); S_V (violet, lambda min-415nm); S_B (blue, 400nm-510nm); S_G (green, 510nm-605nm); S_Y (yellow, 550nm-625nm); S_R (red, 605-lambda max). Vision in *Oophaga pumilio* is trichromatic (λ_{max} LWS = 561, MWS = 489, and SWS = 466 nm).[117]

Pigment Quantification

Frogs were euthanized via decapitation and double-pithing following IACUC protocol (University of Pittsburgh, No. 15106566). Dorsal skin was removed, placed in vials with ~1.5 mL room-temperature Karnovsky's fixative (Morris 1965, pH 7.0–7.2), and, after ~2 hours, replaced with 0.2M sodium cacodylate buffer (pH 7.2) and stored at 4°C. Using a stereomicroscope, up to four 1–2 mm "matchstick" pieces were taken from each skin sample, avoiding melanistic spots. The pieces were postfixed in 1% osmium tetroxide, dehydrated in ethanol, rinsed with propylene oxide, embedded in Epon epoxy resin, and cured at 60°C for at least 48 hours. Thick (1 μ) and thin (350 nm) sections were prepared by histologists at the Center for Biological Imaging (CBI), University of Pittsburgh, and mounted on glass slides.

High-resolution images of one section per matchstick were scanned at 400x magnification using a Zeiss TissueGnostics microscope. Images of unstained sections were re-scanned with a polarizer for overlaying light and polarized images. NIS-Elements and ImageJ software[118] were used to quantify areas of melanins, carotenoids, and reflecting platelets in the dermis. Proportions of total pigment, melanosomes, carotenoids, and reflecting platelets were calculated for each histosection. The counts of the

pigments were transformed using pivot coordinates, a specialized isometric log-ratio transformation.[119] In this method, the first coordinate captures the relative information between two compositional parts (e.g., melanosomes and carotenoids) with respect to the third (e.g., reflecting platelets). This approach enables separate statistical models for each component, isolating their contributions. Data included measurements from 1–4 histosections per individual and 3–5 individuals per morph.

Carotenoid Composition

High-performance liquid chromatography (HPLC) was used on pooled samples of each color morph. Analytical methods followed McGraw[120] with modifications by Crothers et al.[121] for *O. pumilio*. Carotenoids were extracted with a 1:1 hexane/MTBE mixture and analyzed using a Waters HPLC 2695 with a PDA detector 2996. Chromatograms recorded absorbance wavelengths (λ) over retention time (minutes). Peak absorbance wavelengths (λmax) identified pigment types, and the area under each peak estimated pigment quantities (from which concentrations were calculated, as ng pigment per g skin).

Dietary carotenoids can be deposited directly in tissues or enzymatically modified before deposition. These modifications result in three major classes: (1) apocarotenoids, formed by oxidative cleavage of the polyene chain, (2) ε,ε-carotenoids, derived through a β-to-ε shift in the ring double bond and oxidation of the 3-hydroxyl group and (3) ketocarotenoids (4-keto-carotenoids), produced by adding ketone groups at the C4 position which shifts absorption toward the red spectrum.[32,37] Based on these transformations, we categorized carotenoids into five groups: (1) colorless processed carotenoids (apocarotenoids), (2) dietary orange carotenoids (e.g. carotene), (3) dietary yellow carotenoids (e.g. xanthophylls), (4) processed yellow carotenoids (ε,ε-carotenoids), and (5) processed red carotenoids (ketocarotenoids). Morphs were grouped into three categories for analysis: (1) red/orange (n = 5), (2) yellow/green (n = 4), and (3) blue (n = 2), excluding the intermediate/brown Dolphin Bay morph. We plotted the values using *heatmap.2* in R from the *gplots* package.[101] Values were scaled per column and a Z-score was calculated per column. To assess the differences between content of pigments between different color morphs, we performed a SIMPER test in R using the *vegan* package[52] (Table S2).

Probe Design for Exome Capture

The initial transcriptome was 108 Mb represented by 152,862 transcripts.[44] The transcripts were mapped to *the Oophaga pumilio*[43,63,86] and *Ranitomeya imitator* genomes using STARlong 2.7.0d.[102] using the following parameters: –outFilterMismatchNmax 5000, –outFilterMismatchNoverReadLmax.1, –seedSearchStartLmax 20, –seedPerReadNmax 50000, –sjdbOverhang 100 –outFilterScoreMin 0, –outFilterScoreMinOverLread 0, –outFilterMatchNminOverLread.5 –seedPerWindowNmax 1000. We removed the transcripts that did not map to these two assemblies. This resulted in 141,482 transcripts and 104 Mb. Then we used transcript_filter.pl v0.2.0 to remove isoforms. We did two rounds of filtering using the following parameters: 1) minimum 80% coverage and 98% identical 2) 90% coverage, 95% identical. The isoform removal step resulted in 97 Mb. We removed most mitochondrial genes using the annotation and kept cytB. We used 6-Process Annotation (https://github.com/CGRL-QB3-UCBerkeley/MarkerDevelopmentPopGen) to filter out sequences smaller than 150 bp and with a GC content smaller than 35% or larger than 75%. This script also masked repeats setting the parameter to "*Xenopus* genus" and "vertebrates". Finally, we checked whether all candidate color genes were present in our transcriptome. Genes that were missing from the transcriptome were added using their corresponding sequences from the *O. pumilio* or *R. imitator* genomes.The final design had 90 Mb and 115,420 regions and was sent to NimbleGene for approval. NimbleGene made 116,121 probes that targeted 80 Mb, estimating a final coverage of 86 Mb across 110,329 transcripts. The exome capture design is available on Dryad: https://doi.org/10.5061/dryad.np5hqc055.

Library prep

Genomic DNA was extracted from frog tissue samples using the DNEasy Blood and Tissue Kit (Qiagen) according to the manufacturer's protocol for animal tissue. High molecular weight DNA samples from 347 *O. pumilio* individuals were diluted to obtain volumes between 100 and 170 μL with concentrations lower or equal to 30 ng/μL. Samples with similar concentrations and the same volume were grouped in sonication batches. We sonicated using Q800R3 Sonicator from QSonica. We sonicated DNA samples for four minutes, with a pulse of 15 seconds ON / 15 seconds OFF, at 40% amplitude. Tubes were spun down in a centrifuge halfway (after two minutes) and restarted. Samples with low concentration (i.e., <1 ng/μL) were sonicated for an extra minute (five minutes total sonication time; same parameters). Target fragment size was ~300-500bp. We verified that the sonication worked properly by running 1 μL of each sample on a 2% agarose gel.

Sonication was followed by size selection using lab-made SPRI beads [20% PEG-8000 / 2.5M NaCl / 1 mg/mL Sera-Mag Speed-Bead Carboxylate-Modified Magnetic Particles (Hydrophobic) 65152105050250[122]] to refine the fragment sizing. These magnetic beads reversibly bind to larger or smaller sized DNA fragments depending on the volume added. The target for our libraries was ~350 bp, so we used a 0.5x ratio for the right-side selection and 0.65x for the left-side. We used the Rainin Benchsmart 96, a high-throughput pipetting system, to treat 96 samples simultaneously. Each plate had randomly selected samples from different populations. An agarose gel was run after the double-sided bead cleaning to confirm the fragment sizes. Then, we used a modified Kapa HyperPrep library prep kit for end repair and A-tailing,[123] followed by adapter ligation with a universal stub. The next step was a post-ligation bead clean-up to remove excess adapters and ligase. Finally, we performed a 0.8x SPRI cleaning on the Benchsmart.

The final stage of library preparation was to use long, TruSeq-style indexing oligos to amplify the libraries in order to: 1) enrich for fragments with adapter ligated on both ends, 2) to extend the length to anneal to the Illumina flowcell, and 3) to incorporate a unique dual-index molecular tag so that the reads associated with the 347 pooled libraries could later be separated during demultiplexing.

Please cite this article in press as: Aguilar-Gómez et al., Selection-driven color variation in the aposematic strawberry poison frog, *Oophaga pumilio*, Current Biology (2026), https://doi.org/10.1016/j.cub.2026.01.041

We used plates provided by the Functional Genomics Laboratory (University of California, Berkeley) that contain 5 μL of a pre-mixed unique P5 and P7 indexing oligos for each sample. To this we added 15 μL of Kapa 2x HiFi HotStart ReadyMix and 10 μL of our adapter-ligated product. Then this was given 8-10 cycles (depending on DNA input mass) of indexing PCR according to the standard Kapa Hyper Prep gDNA protocol. Amplification involved initial denaturation at 98°C for 45 seconds. This was followed by 8-12 cycles (depending on DNA quantity) of denaturation at 98°C for 15 seconds, annealing at 60°C for 30 seconds, and extension at 72°C for 60 seconds. A final step of DNA extension lasted 5 minutes at 72°C. The Benchsmart was again used to do a final 0.8x bead clean-up to remove excess indexing oligos and dimers. After completing the libraries, we did quality control by measuring the final concentration using a Qubit fluorimeter and running agarose gels and Bioanalyzer DNA 1000 chips to obtain library sizing information. After adding the adapter and index, the average size of libraries was ∼450-650 bp.

Pooling and Exome Capture

For the capture hybridization we made five pools containing ∼70 samples each: we pipetted different volumes per sample depending on the concentration to ensure we had the same mass for each sample (150 ng). Each pool consisted of samples from different populations and contained a total of ∼3 μg of DNA. We added 15 μL of blocking oligos (Roche UBO), 5 μL of Cot-1 from each of three different species (human, mouse, chicken), and 15 μL of Roche Developer Reagent. Then we concentrated the pools in a vacuum centrifuge and resuspended the pools in Roche Nimblegen buffers 5 and 6. We aliquoted the Nimblegen probes into strip tubes, added the DNA mix to the probes, denatured at 95°C, and started hybridizing at 47°C. We incubated for 72 hours and 45 minutes. [Aside from starting with higher library mass, incorporating additional blocking elements (both due to the larger genome size of *Oophaga pumilio*), and the longer hybridization time, we followed the Roche SeqCap EZ HyperCap Workflow User's Guide v2.0 protocol as written.] After probe hybridization, we followed the Nimblegen protocol to bind the probes to streptavidin-coated beads (Dynabeads M270, Thermo Scientific), thoroughly wash the beads/probe/library complex, and elute the captured DNA. 20 μL of bead-bound captured product was used as template for enrichment PCR and added to 25 μL Kapa 2x HiFi HotStart ReadyMix and 5 μL Kapa 10x Illumina Primer Mix. This was given 10 cycles of amplification according to the EZ HyperCap v2.0 protocol and each capture product was amplified separately in three different reactions. These were cleaned with a 1.0x ratio of SPRI beads, eluted in 20 μL and then the three reactions for each pool were combined. We assessed the final concentration, size distribution, and quality of the amplified captured pools using Qubit fluorimeter values, Bioanalyzer, and agarose gel electrophoresis.

Sequencing and Read processing

We sequenced two lanes of Illumina NovaSeq 6000 150PE Flow Cell S4 at the Vincent J. Coates Genomics Sequencing Laboratory ("QB3 Genomics, UC Berkeley, Berkeley, CA, RRID:SCR_022170"). We used *Trimmomatic-0.39*[103] to remove adapters (ILLUMINACLIP:TruSeq3-PE.fa:2:30:10), leading and trailing low quality or N bases (below quality 3) (LEADING:3,TRAILING:3), cut reads when the average quality per base drops below 15 in a 4-base sliding window (SLIDINGWINDOW:4:15), and drop reads below the 75 bases long (MINLEN:75). We also used PRINSEQ-lite 0.20.4 to remove low complexity reads (-lc_method dust -lc_threshold 7) and overrepresented sequences (-custom_params "G 50").

Mapping and annotation

The reads from each sequencing lane were mapped independently to the *O. pumilio* rescaffolded genome, (referred to in the main text as "fragmented *O.pumilio* assembly") [total length: 4,837,165,062 bp/ L50: 11,434/ N50: 105,380 bp][43,46] using BWA-MEM version 0.7.17.[104] Next, we filtered the alignments with SAMtools 1.11[105] and used the flag -F 1804 to exclude reads: read unmapped (0x4), mate unmapped (0x8), non-primary alignment (0x100), read fails platform/vendor quality checks (0x200), and read is PCR or optical duplicate (0x400). Finally, we merged the BAM files coming from different lanes for each individual. The publicly available rescaffolded genome[43] was not annotated, so we used the coordinates of the mapped transcriptome to the *O. pumilio* (see section Probe design for exome capture) as annotation. Later, we contacted the author of the rescaffolded genome[43] and he kindly provided the gff file, without gene names. For all the labeled genes, the CDS was extracted using GffRead[106] and blasted against the nucleotide database.[124] We made sure all genes corresponded in both annotations.

SNP filtering

SNP filtering was performed using ANGSD *0.941-13-gb7eb654*.[107] We kept SNPs with a minimum of 250 individuals with 1x depth (minInd, setMinDepthInd), maximum depth of 50x (setMaxDepthInd), base quality 25 (minQ), mapping quality 25 (minMapQ), polymorphic sites p-value<1e-6 (SNP_pval), remove triallelic sites and use the reference genome as major (skipTriallelic, doMajorMinor), discard reads with flag >=256 (remove_bads), discard reads that do not map uniquely (uniqueOnly), keep only paired-end reads that mapped correctly (only_proper_pairs). We also removed SNPs with excess heterozygotes (hetbias_pval 1e-6), strand bias (sb_pval 1e-4), end distance bias (edge_pval 1e-4), and map quality bias (mapQ_pval 1e-4). This filtering resulted in 10,231,695 sites. These sites have an average depth of 8.22x.

Population Structure Analyses

A 5% minor allele frequency was implemented to run the population structure analyses. We obtained 1,973,099 SNPs after this filter. We used *PCAngsd 1.10*[125] to perform Principal Component Analysis (PCA). The program *qpas* from *OHANA*[47] was used to calculate

Please cite this article in press as: Aguilar-Gómez et al., Selection-driven color variation in the aposematic strawberry poison frog, *Oophaga pumilio*, Current Biology (2026), https://doi.org/10.1016/j.cub.2026.01.041

ancestry components with k=4 to k=10. We sampled randomly 1% of the sites to calculate ancestry components. We calculated the covariance of the allele frequencies in different components using *nemeco* from *OHANA*[47] to approximate a tree.

Demographic Inference

We generated a binary vcf file using the command -doBcf 1 from ANGSD[107] and -doGeno 3, and -doPost 1 using the same filters as described in the SNP filtering section, but including the two outgroup samples (*O. sylvatica*). We converted the vcf file to plink format with –maf 0.0057 to make sure we included variants that are present in at least 2 individuals (2/349); this resulted in 1,982,428 variants. We converted the plink format into TreeMix[108] format, which is the same format needed in AdmixtureBayes.[48] We ran AdmixtureBayes on the input file for TreeMix when allowing for each of 0, 1, 2, 3, and 4 admixture events, and obtained a distribution of admixture graphs for each number of events. Three independent MCMC chains were run for each analysis, and convergence was assessed through both trace plot analysis and Gelman-Rubin convergence diagnostics to verify that the stationary distribution had been reached. Each chain was run with the parameters –n 750000 –MCMC_chains 31 –spacing 1.4 –maxtemp 1000 –max_admixes k –num_ind_snps 40000, where k denotes the number of admixture events that were allowed. For the *analyzeSamples* step, a burn-in fraction of 0.3 and a thinning rate of 10 were used to obtain our sample of graphs from the stationary distribution.

To test the performance of AdmixtureBayes with parameters resembling the *O. pumilio* dataset, we ran a set of simulations to check the self-consistency of the AdmixtureBayes results. In particular, we ran simulations with both 0 admixture events and 1 admixture event with branch lengths and admixture proportions that matched those that were inferred by AdmixtureBayes on the real dataset. Mutation rates and sample numbers in each population were set to match the real data. For each simulation, a 50Mb region was simulated in msprime[109] with a mutation rate of 2 x 10 ^(-9) and a recombination rate of 10 ^(-8). Sample sizes for each population were chosen to match the real dataset: 3 from PD, 35 from TB, 30 from HP, 15 from CL, 63 from CM, 34 from PO, 7 from RA, 26 from SC, 104 from DB, 30 from SK, and 4 from the outgroup. The branch lengths for the 0 admixture event simulations can be represented by the Newick Tree: (((((((((SK:0.000000012,DB:0.0064):0.026,SC:0.2367):0.0183,RA:0.024):0.139,PO:0.102):0.0182,(CL:0.0767,CM:0.176):0.033):0.046,HP:0.141):0.0246,(PD:0.044,TB:0.176):0.064):0.115,outgroup:0.115); and the branch lengths and admixture proportions for the 1 admixture event simulations can be represented by the Newick tree: (((((((SK:0.00001228429,DB:0.0064):0.0266,SC:0.2362):0.0174,RA:0.0246):0.1298,((HP2:0.1474,CM:0.126):0.0596,CL:0.0652):0.0489):0.027,PO:0.0887):0.0628,((TB:0.14119,HP1:0.1625):0.04725,PD:0.0315):0.066):0.115,outgroup:0.115); followed by HP1 and HP2 admixing with an admixture proportion of 0.5 each and the resulting HP population having a terminal branch length of 0.07598. For each number of admixture graphs (0 and 1), 20 independent 50Mb regions were generated. AdmixtureBayes was run on each with the arguments –n 20000 and –max_admixes k for k = 0 or k = 1. All other parameters were left to their default values. For each dataset, we examined the tree that was sampled with the highest posterior and also examined 100 trees sampled from the posterior distribution. For each tree, we calculated the topology equality, which is 1 if the topology matches the simulated topology and 0 otherwise. We considered the distribution of the topology equality for the tree with the highest posterior (which we call the mode) across all 20 datasets and do the same for the average value of the topology equality over all 100 samples trees from the posterior (which we call the mean). Across both the mode and mean and both 0 and 1 admixture events, we find all topology equality metrics to be > 0.99, indicative of strong concordance between the inferred and true topologies. All simulation scripts can be found in the AdmixtureBayesSimulations folder of the 7_Demography directory on the accompanying GitHub (https://github.com/aguilar-gomez/pumilioAnalysis/).

We calculated the folded 2dsfs using *realSFS*[107] and ran *dadi*[49] with pairs of populations using two models: 1) population split and 2) population split with migration. The mutation rate was set to 10^{-9}, per year and the generation time was set to two years.[20] The total length of DNA sequence analyzed to obtain the SNP data (10,788,793 bp) was set to 164,229,310 bp, which includes invariant sites. This number was obtained from mapping the exome capture data to the whole genome and keeping only positions that passed the following thresholds: 250 individuals with 1x depth (*minInd, setMinDepthInd*), maximum depth of 50x (setMaxDepthInd), base quality 25 (*minQ*), and mapping quality 25 (*minMapQ*). We generated the folded joint SFS for each pair of populations using *realSFS*. We ran the program 100 times for each pair of populations and selected the model with the highest log-likelihood. We used the split with migration model, which has the following parameters: population sizes (nu1,nu2), time of the split (T), and migration rates (m12, m21, we used symmetric migration). The initial parameters for the models were (params = [1,1,1,1], lower_bounds = [1e-3, 1e-3, 1e-3, 1e-5], upper_bounds = [200,200, 300, 100]). For the model with no migration, we used the same parameters and set m12=m21=0. We used the method (dadi.Misc.perturb_params) to perturb the parameters for each run.

Synteny alignment

We aligned the genome of *O. sylvatica*, which was provided by the group of Lauren O'Connell from Stanford University (now publicly available SRA: PRJNA909817), and the rescaffolded *Oophaga pumilio* genome.[43] The alignment was performed with *nucmer* from MUMmer4,[110] which aligns the two genomes using a minimum cluster length (-c 2000), ten threads (-t 10), and used FASTA files as input. The alignment results are filtered with *delta-filter*[110] to retain only high-confidence one-to-one alignments with at least 95% identity. The filtered data is then processed using a Python script to create a layout file for visualization, which is split into a reference layout containing chromosome names and lengths, and a query layout listing the sequences to be visualized. Finally, the *mummerplot* tool generated a PNG plot of the alignment, using the layout and filtered alignment data. The output of the *layout.py* script provided a

one-to-one correspondence between the scaffolds of *O. pumilio* and chromosome level genome of *O. sylvatica*. For plotting using the synteny, we organized the scaffolds according to the layout output; scaffolds that did not have a confident match are plotted at the right from the chromosomes.

Coding mutations and protein trees

We generated a consensus fasta sequence per population (-doFasta 2 from ANGSD[107]). Then we used the gff3 file to extract the CDS and compare the sequences between morphs. We obtained the synonymous and non-synonymous mutations in the candidate genes. We explored the structure of the protein changes using SWISS-MODEL[60] (https://swissmodel.expasy.org/). We aggregated the consensus CDS from each population in a single file. Since they were generated from the same coordinates, putting all the sequences in the same fasta file worked as an alignment. We generated a tree with the neighbor joining algorithm in Jalview[114] using the aggregated fasta as input.

Average genomic tree and gene trees

The gene trees with each individual having its own branch were generated using genotype likelihoods as described in Jin et al.[29] and briefly described next; for the average genomic tree, we used the 10,231,695 sites described in SNP filtering. We used the sites passing the filters that fall within the corresponding scaffold. All the trees generated for genes of interest had only one gene per scaffold. We calculated the distances using ngsDist[115] with genotype likelihoods. We implemented neighbor-joining (BIONJ) FASTME 2.1.6.2[116] to infer the trees. All the trees are unrooted.

4-population (ABBA-BABA) test

We used ANGSD *0.941-13-gb7eb654*[107] to perform a 4-population test (ABBA-BABA test) using the -doAbbababa2 function (Data S1). This test evaluates deviations from a strictly bifurcating tree topology by quantifying excess allele sharing among populations. We provided a list of BAM files containing aligned sequencing reads and population size information. Analyses were restricted to a predefined set of genomic regions using both a region file (-rf) and a site file containing variant positions (-sites) (see SNP filtering). To ensure high-quality site representation, we included only uniquely mapping reads (-uniqueOnly 1) and removed triallelic sites (-rmTrans 0). We mapped *O. sylvatica* reads (kindly provided by Lauren O' Conelll) to the *O. pumilio* genome to generate a BAM file that was used as an outgroup for all the test.

qPCR experimental methods

We extracted total RNA from skin tissue samples preserved in RNAlater. Tissues were homogenized using 2 mL tubes pre-filled with 2.8 mm ceramic beads in a bead mill homogenizer. RNA was purified with the Monarch Spin RNA Isolation Kit (NEB #T2110) following the manufacturer's protocol, including on-column DNase I treatment to remove genomic DNA. RNA concentration and quality were assessed using Qubit, and all procedures were performed under RNase-free conditions. Reverse transcription was carried out using the SuperScript IV VILO Master Mix (Invitrogen) as part of a two-step RT-qPCR workflow. cDNA synthesis reactions contained 250 ng of total RNA in a 20 μL volume and used a mixed priming strategy consisting of oligo(dT)$_{\backslash 18}$ and random hexamers. No-RT controls were included for each sample. The thermal protocol consisted of 25°C for 10 min (primer annealing), 50°C for 10 min (cDNA synthesis), and 85°C for 5 min (enzyme inactivation). Quantitative PCR was performed in 20 μL reactions containing 10 μL SYBRGREEN Select Master Mix (Applied Biosystems), 1 μL each of 5 μM forward and reverse primers (final concentration 250 nM), 2 μL of 1:10 diluted cDNA, and nuclease-free water. Cycling consisted of 50°C for 2 min (UDG activation), 95°C for 2 min (polymerase activation), followed by 40–45 cycles of 95°C for 15 s, 55°C for 15 s, and 72°C for 30 s, and concluded with a melt-curve analysis (95°C for 15 s, 55°C for 1 min, then ramping to 95°C at 0.15°C/s). Primers were designed in Primer3 based on coding sequence transcript alignments to Oophaga pumilio scaffolds in Geneious and were placed across exon–exon junctions near the 3′ end of transcripts to ensure amplification of cDNA rather than genomic DNA.

QUANTIFICATION AND STATISTICAL ANALYSIS

qPCR statistical methods

To calculate the gene expression ratio, we used the Pfaffl method,[126] which considers primer efficiencies (E). We calculated each sample's average and standard deviation CT in the gene of interest (GOI) and reference gene (REF). The ΔCT was calculated using a reference sample in all plates.

We used the following formula to calculate the gene expression ratio:

$$expRatio = \frac{E_{GOI}^{\Delta CT_{GOI}}}{E_{REF}^{\Delta CT_{REF}}}$$

And we calculated the standard error (SE) to add error bars:

$$SEexpRatio = expRatio * \sqrt{Var\Delta CT_{GOI} * log(E_{GOI})^2 + Var\Delta CT_{REF} * log(E_{REF})^2}$$

Please cite this article in press as: Aguilar-Gómez et al., Selection-driven color variation in the aposematic strawberry poison frog, *Oophaga pumilio*, Current Biology (2026), https://doi.org/10.1016/j.cub.2026.01.041

Selection scans and genomic associations

We calculated the population divergence using *realSFS*[127] to estimate the fixation index F_{ST}. We performed selection scans by calculating the Population Branch Statistic (PBS) by windows across the genome using *realSFS*. We calculated the unfolded 2dsfs of the three pairs of each combination. We obtained a global estimation of F_{ST} (Table S1) and PBS, followed by window estimation (size=100,000 bp, step=20,000 bp). We excluded incomplete windows. We annotated the 99.8th outliers with windows with at least 20 SNPs. Windows were annotated with a gene name if they overlap with the gene annotation; we kept the label on the window with the highest PBS value for each gene.

Genomic associations were performed on spectrophotometer measurements of light wavelengths. We used GEMMA 0.98.5[111] to perform a Wald test using a standardized relatedness matrix (calculated with GEMMA). To identify related individuals, we estimated pairwise relatedness within each population using ngsRelate2,[128] which relies on genotype likelihoods (Data S2). Individuals with relatedness $r > 0.1$ were considered related. This resulted in 32 related pairs; to avoid inflating association signals, we removed 26 individuals, retaining only one individual per related pair in the GWAS.

To reduce the number of SNPs displayed in the Manhattan plots, we excluded SNPs with p-value > 0.1. From the surviving SNPs, we annotated SNPs in the 99.98th percentile of the test statistic distribution and retained only genes containing at least two outlier SNPs. SNPs were assigned to genes only if they fell within annotated gene boundaries, including introns. To visualize genomic context, we aligned the *O. pumilio* genome to the contig-level *O. sylvatica* assembly and plotted scaffold positions according to this synteny map.

The inflation factor (λ) was calculated by transforming p-values from the Wald test into chi-square statistics using the inverse chi-square cumulative distribution function with one degree of freedom. Then, the factor was computed as the ratio of the empirical median to its theoretical expectation under a chi-square distribution with one degree of freedom. The chi-square statistics were then adjusted by this factor to correct for inflation, and the corrected values were converted back to p-values using the chi-square survival function. Values of λ greater than 1 indicate inflation due to unaccounted structure or relatedness, whereas values less than 1 indicate deflation, which may arise from overcorrection or limited power. In our analyses, λ was 0.70 (blue), 0.93 (red), and 0.85 (green), all below 1 and therefore indicative of slight deflation rather than inflation. Following best practices, we corrected test statistics using the maximum of λ and 1; because all λ values were < 1, no inflation correction was applied. We note this explicitly to clarify that the observed Q–Q patterns do not reflect inflation.

The proportion of genetic variance among populations explained by the top associated SNP variants in each association peak was estimated using the following formula according to Zhou et al.[129]

$$PVE = \frac{\sigma^2_{gen} * \left(\beta^2 + SE^2\right)}{\sigma^2_{phe}}$$

Where σ^2_{gen} is calculated using the allele frequency (af) of the SNP σ^2_{gen}= 2*af(1-af). The effect size (β) and its standard error (SE) are calculated for each SNP by GEMMA. The phenotypic variance (σ^2_{phe}) was calculated using the reflectance values per population.

Differential expression

Publically available RNA-seq skin cell dataset from five green, five red, and five blue Bocas del Toro *O. pumilio*[43] was downloaded using fasterq-dump from NCBI.mTrimmomatic (v0.39) parameters: "2:30:10:2:keepBothReads LEADING:3 TRAILING:3 MINLEN:75" was used to remove adapters. We generated a gtf file using gffread[106] (v0.12.7) from the gff annotation without gene names provided by the author of the publicly available dataset. We used STAR's[102] "–runMode genomeGenerate" function to index the genome using the following parameter "–limitGenomeGenerateRAM 4272279470500 –genomeSAindexNbases 15.086". Afterwards, we aligned the reads to the indexed reference genome using STAR (v2.7.10): "–runMode alignReads" with parameter "–readFilesCommand zcat –quantMode TranscriptomeSAM". Transcript quantification was done using RSEM v1.3.3. with rsem-prepare-reference followed by rsem-calculate-expression.

For the annotation, we used TransDecoder[112] (v5.5.0)'s gff3_file_to_bed.pl to transform the gff file into a bed file. We blasted all the transcripts to the Blast Nucleotide Database[130] since the gff was provided without gene names. We kept the gene name annotation for each transcript with the highest bitscore. For our genes of interest, we also corroborated the annotation of the transcripts and the genome assembly location using our assembly annotation. We ran differential expression analysis with DESeq2[113] in R (v4.2.0), using RSEM 'expected_counts' as input. All differential expression analyses were performed using DESeq2 size-factor–normalized counts derived from RSEM expected counts. Transcripts were aggregated by gene name. We subset to only candidate genes that were outliers of selection - color association genomic scans. We did all the pairwise combinations (blue-red-green) and ran the DESeq2 analysis function. We kept the significant DE genes (q-value<0.05).

Haplotype divergence estimation

We estimated haplotype divergence between two morphs within the target gene region by first calculating site allele likelihoods for shared segregating sites using *ANGSD* with the -doSaf 1 option. We then computed the two-dimensional joint site frequency spectrum (2D SFS) using *realSFS*. Pairwise nucleotide divergence (π_{12}) between the two morphs was calculated from the 2D SFS using the expected number of differences between alleles sampled from each morph. Specifically, for each bin (i,j)in the

Please cite this article in press as: Aguilar-Gómez et al., Selection-driven color variation in the aposematic strawberry poison frog, *Oophaga pumilio*, Current Biology (2026), https://doi.org/10.1016/j.cub.2026.01.041

2D SFS, where i and j represent the number of derived alleles in morphs 1 and 2, respectively, and n_1, $n_2$are the number of alleles per morph, we used the formula:

$$\pi_{12} = \sum_{i=0}^{n1} \sum_{j=0}^{n2} SFS_{ij} \cdot \frac{i(n2 - j) + j(n1 - i)}{n1n2}$$

Finally, divergence time for the gene of interest dT_{goi} was estimated as:

$$dT_{goi} = \frac{\pi_{12}}{2\mu S}$$

Where $\mu = 10^{-9}$is the mutation rate per site per year, and S is the number of shared segregating sites between the two morphs in the gene region.

HKA test

We used the HKA test[131] to assess whether the genes we found involved in pigmentation have neutral evolution patterns. We calculated the allele frequencies using ANGSD (-doMaf 1)[132] and the allele in the reference genome as major (-doMajorMinor 4). We kept non-variable sites and biallelic variants that passed the above SNP filtering. We compared *O. pumilio* population allele frequencies against the outgroup *R. imitator*. A site was defined as polymorphic when segregating (.001< af1 <.999) in the population of interest and fixed (af2 <.001 or af2 >.999) in the outgroup. A site was defined as fixed if the population and the outgroup were fixed for different alleles. By adding a divergent outgroup, some of our biallelic SNPs in *O. pumilio* were triallelic, with a different allele in *R. imitator*. We also counted a site as both fixed and polymorphic if it was segregating in *O. pumilio* and fixed for a third allele in the outgroup.

We counted all the fixed and polymorphic sites genome-wide. We built a contingency table comparing the fixed and polymorphic sites within a scaffold compared to genome-wide counts and performed a X^2 test using Yates correction. We adjusted the X^2 values using genomic control and calculating a deflation/inflation index.

Tajima's D

We calculated site allele frequency likelihood using *doSaf -1* of all the sites that passed the SNP filters and the invariable sites that passed the mapping and read quality filters. Then we calculated the maximum likelihood estimate of the folded site frequency spectrum (*realSFS*) and thetas estimate for each site using saf2theta.[133] The output of this method gives estimates of nucleotide diversity (Pairwise: tP) and Watterson theta (Watterson; tW). We calculated Tajima's D according to the formula described in Tajima[134]:

$$D = \frac{tP - tW}{\sqrt{e_1 S + e_2 S(S - 1)}}$$

where S is the number of segregating sites and e_1 and e_2 are variance estimators. We performed the calculations using windows of 1000 sites. The scripts used can be found here: https://github.com/aguilar-gomez/angsdSupplement/

Current Biology, Volume *36*

Supplemental Information

Selection-driven color variation in the aposematic strawberry poison frog, *Oophaga pumilio*

Diana Aguilar-Gómez, Layla Freeborn, Lin Yuan, Lydia L. Smith, Alex Guzman, Andrew H. Vaughn, Emma Steigerwald, Adam Stuckert, Yusan Yang, Tyler Linderoth, Matthew MacManes, Kevin J. McGraw, Corinne L. Richards-Zawacki, and Rasmus Nielsen

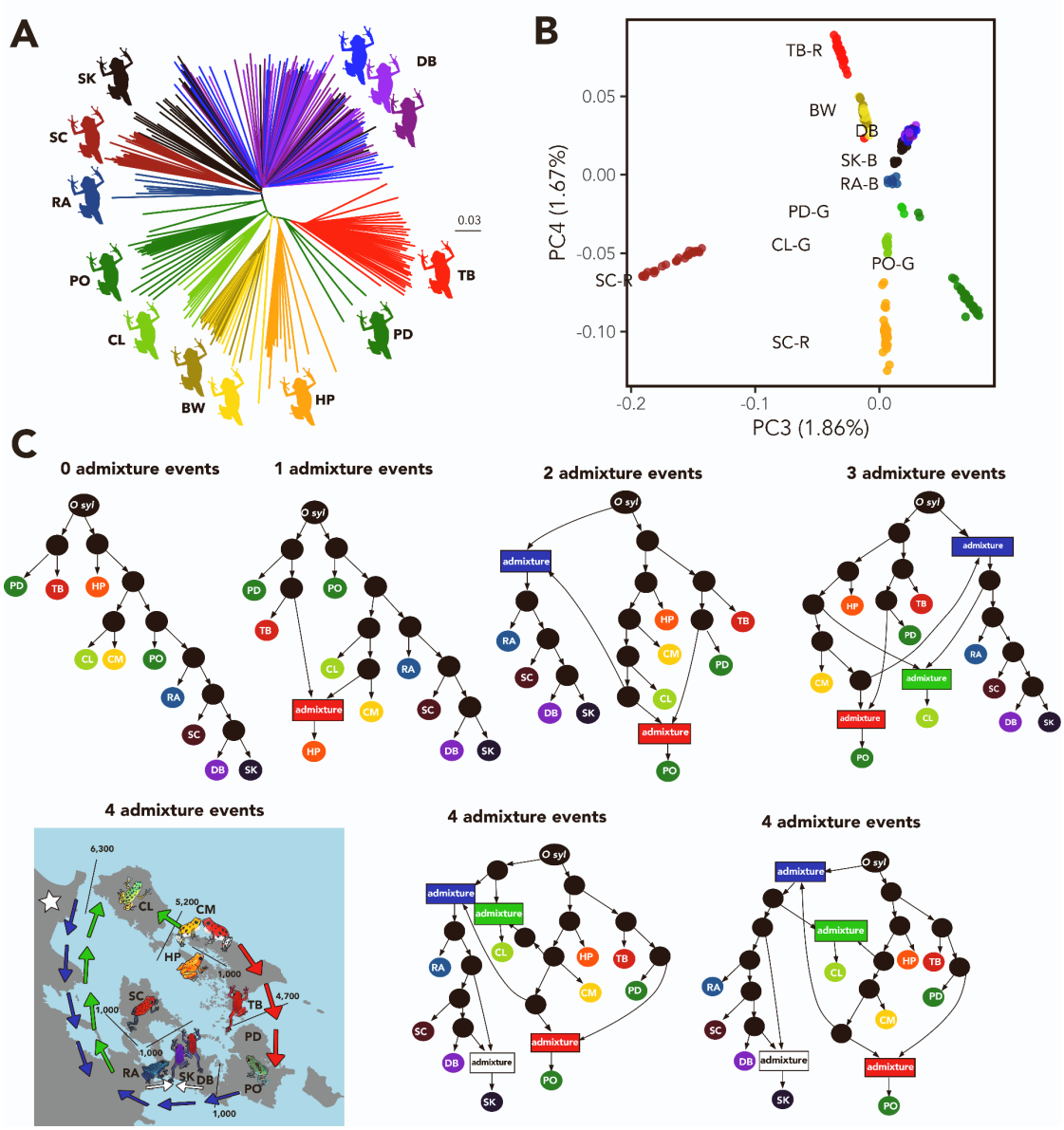

Figure S1. Additional population structure and admixture graph inference results. Related to Figure 1. A) Genome-wide tree. Population abbreviations are the same used in Figure 1: DB (Dolphin Bay), SK (Shark Hole), RA (Rana Azul), PO (South Popa), CL (Colon), BW (Bastimentos West), HP (Hospital Point), PD (North Popa), SC (San Cristóbal), and TB (Tranquilo Bay); B) Additional PCA components. PC3 and PC4 with the variance they explain in parentheses. Colors in panel B correspond to the same population colors shown in A. C) Additional topologies and their probabilities given the number of migration events. 0 events (100%), 1 event (100%), 2 events (100%), 3 events (68%, 32% [not shown]), and 4 events (45% [shown in Figure 1E], 17%, 12% [not shown]). The probability of these three topologies is 74% of all sampled graphs with 4 migration events; the rest of the topologies each have 1-3% probability and are not shown here. Population abbreviations are the same used in Figure 1: DB (Dolphin Bay), SK (Shark Hole), RA (Rana Azul), PO (South Popa), CL (Colon), BW (Bastimentos West), HP (Hospital Point), PD (North Popa), SC (San Cristóbal), and TB (Tranquilo Bay). The map shows the time of the most recent split of the islands in years, and the arrows show inferred gene flow matching the colors to the admixture events. The white star shows the inferred ancestral population of all the islands.

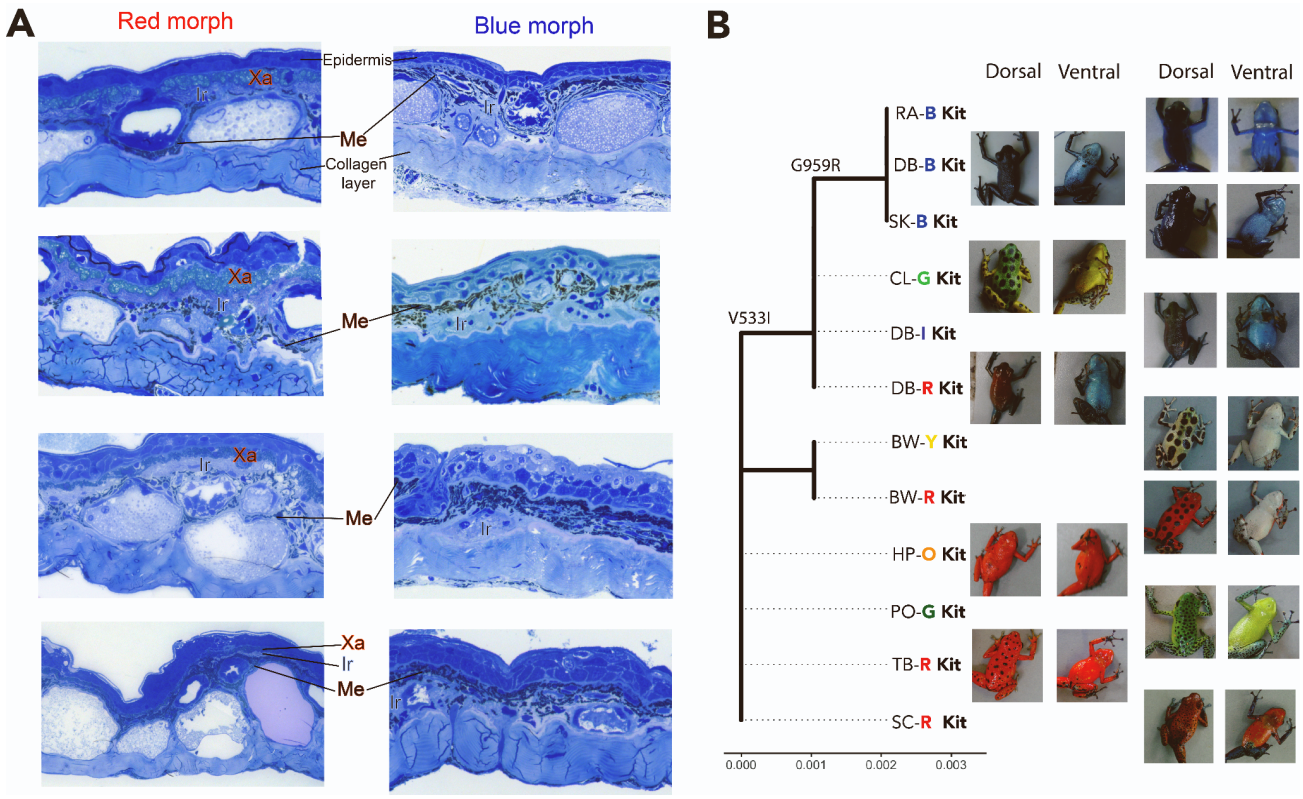

Figure S2. Chromatophore Layering and Kit Amino Acid Variation Underlying Blue Coloration in Oophaga pumilio. Related to Figure 3. A) Representative transverse sections of *O. pumilio* skin stained with toluidine blue show the organization of the epidermis, collagen layer, and the three major chromatophore types: melanophores (Me), iridophores (Ir), and xanthophores (Xa). Melanophores contain melanosomes, iridophores contain reflecting platelets, and xanthophores contain carotenoid pigments. Red morphs exhibit abundant xanthophores and more deeply positioned melanophores, with iridophores distributed beneath them. In contrast, blue morphs show a dense band of melanophores located immediately beneath the epidermis, reduced xanthophores, and iridophores arranged in a more compact layer directly below the melanophores. These differences in chromatophore abundance and layering are consistent with pigment-based red coloration versus structurally enhanced blue coloration. B) A protein tree of Kit. Population abbreviations are: DB (Dolphin Bay), SK (Shark Hole), RA (Rana Azul), PO (South Popa), CL (Colón), BW (Bastimentos West), HP (Hospital Point), PD (North Popa), SC (San Cristóbal), and TB (Tranquilo Bay). Distance is shown on the x-axis and amino acid changes are shown next to the branches they affect. On the right, we present pictures of dorsal and ventral skin of a representative individual from each population.

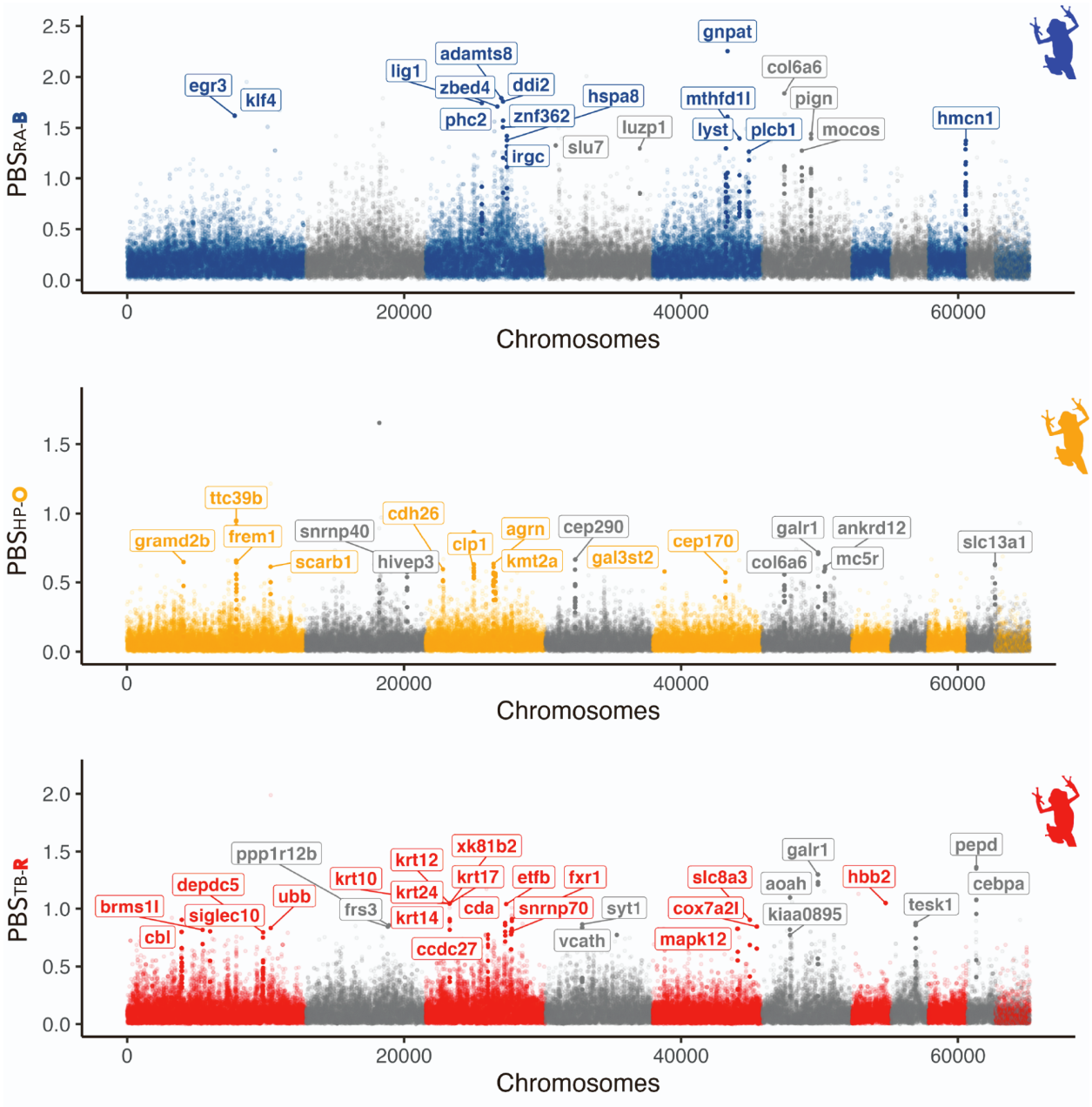

Figure S3. Additional PBS scans. Related to Figures 3,4 and 5. From top to bottom: Branch of Rana Azul blue frogs (RA-B) vs Bastimentos West morphs (BW-R and BW-Y); Branch of Hospital Point orange frogs (HP-O) vs Colon (CL-G) and South Popa (PO-G) green frogs; Branch of Tranquilo Bay red frogs (TB-R) vs Shark Hole blue (SK-B) and South Popa green (PO-G).

	SK	RA	CL	BWR	BWY	DBB	DBI	DBR	HP	PD	PO	SC	TB
SK	-	0.054	0.126	0.194	0.193	0.012	0.011	0.012	0.178	0.191	0.124	0.132	0.202
RA	0.054	-	0.137	0.207	0.208	0.06	0.058	0.06	0.177	0.193	0.125	0.146	0.187
CL	0.126	0.137	-	0.134	0.135	0.131	0.127	0.131	0.134	0.183	0.114	0.281	0.173
BWR	0.194	0.207	0.134	-	0.009	0.199	0.188	0.202	0.152	0.232	0.156	0.281	0.21
BWY	0.193	0.208	0.135	0.009	-	0.197	0.186	0.2	0.152	0.234	0.155	0.279	0.207
DBB	0.012	0.06	0.131	0.199	0.197	-	0.009	0.01	0.182	0.194	0.13	0.137	0.207
DBI	0.011	0.058	0.127	0.188	0.186	0.009	-	0.008	0.178	0.192	0.128	0.135	0.206
DBR	0.012	0.06	0.131	0.202	0.2	0.01	0.008	-	0.183	0.195	0.131	0.136	0.207
HP	0.178	0.177	0.134	0.152	0.152	0.182	0.178	0.183	-	0.159	0.142	0.253	0.154
PD	0.191	0.193	0.183	0.232	0.234	0.194	0.192	0.195	0.159	-	0.139	0.257	0.126
PO	0.124	0.125 281	0.114	0.156	0.155	0.13	0.128	0.131	0.142	0.139	-	0.222	0.164
SC	0.132	0.146	0.195	0.281	0.279	0.137	0.135	0.136	0.253	0.257	0.222	-	0.271
TB	0.202	0.187	0.173	0.21	0.207	0.207	0.206	0.207	0.154	0.126	0.164	0.271	-

Table S1. Pairwise F_{ST} between Bocas del Toro morphs. Related to Figure 1 and STAR Methods. Population abbreviations are the same used in Figure 1: SK (Shark Hole), RA (Rana Azul), CL (Colón), BW (Bastimentos West; BWR: red, BWY:yellow), DB (Dolphin Bay; DBB: blue, DBR: red, DBI:intermediate), HP (Hospital Point), PD (North Popa), PO (South Popa), SC (San Cristóbal) and TB (Tranquilo Bay).

A	B	species	Av	Sd	Ratio	Av A	Av B	Cum Sum	Perm p-value
Red orange	Yellow green	colorless processed pigment	0.017	0.01	1.40	4.80	3.28	0.634	0.921
Red orange	**Yellow green**	**dietary orange pigment**	**0.515**	**0.19**	**2.68**	**143.38**	**6.23**	**0.783**	**0.020**
Red orange	**Yellow green**	**dietary yellow pigment**	**0.039**	**0.01**	**2.99**	**10.05**	**0.67**	**0.930**	**0.030**
Red orange	Yellow green	processed yellow pigment	0.119	0.08	1.43	34.77	8.57	0.979	0.980
Red orange	**Yellow green**	**ketocarotenoid**	**0.121**	**0.06**	**1.94**	**27.56**	**1.94**	**1.000**	**0.020**
Red orange	Blue	colorless processed pigment	0.006	0.00	1.39	4.80	3.90	0.615	1.000
Red orange	**Blue**	**dietary orange pigment**	**0.589**	**0.17**	**3.44**	**143.38**	**0.00**	**0.795**	**0.020**
Red orange	**Blue**	**dietary yellow pigment**	**0.046**	**0.01**	**3.83**	**10.05**	**0.00**	**0.945**	**0.020**
Red orange	Blue	processed yellow pigment	0.172	0.09	1.91	34.77	0.16	0.994	0.337
Red orange	**Blue**	**ketocarotenoid**	**0.144**	**0.07**	**2.01**	**27.56**	**0.00**	**1.000**	**0.020**
Yellow green	**Blue**	**colorless processed pigment**	**0.181**	**0.10**	**1.76**	**3.28**	**3.90**	**0.403**	**0.010**
Yellow green	Blue	dietary orange pigment	0.186	0.16	1.16	6.23	0.00	0.638	0.990
Yellow green	Blue	dietary yellow pigment	0.019	0.02	1.18	0.67	0.00	0.865	0.960
Yellow green	**Blue**	**processed yellow pigment**	**0.320**	**0.21**	**1.50**	**8.57**	**0.16**	**0.976**	**0.010**
Yellow green	Blue	ketocarotenoid	0.088	0.04	2.48	1.94	0.00	1.000	0.634

Table S2. SIMPER test results showing carotenoid differences between O. pumilio color morphs. Related to Figure 2 and STAR Methods. Morphs were grouped into three groups for these tests: 1) red/orange, 2) yellow/green and 3) blue; intermediate color morphs were excluded (blue-red intermediate).

Carotenoid Pigment	B	S_R	S_Y	S_G	S_B	S_V
Apocarotenoid	ns	+ **	ns	- ***	ns	ns
Canary Xanthophyll Ester 1	+ *	+ **	ns	ns	- *	- *
Canary Xanthophyll Ester 2	+ *	+ **	ns	ns	- *	- *
Canary Xanthophyll Ester 3	ns	+ **	ns	ns	- *	- *
Echinenone	ns	ns	ns	ns	ns	ns
Canthaxanthin Ester 1	ns	+ *	ns	ns	ns	ns
Canthaxanthin Ester 2	ns	+ *	ns	ns	ns	ns
B-carotene	+ ***	+ ***	ns	ns	- **	- **
Ketocarotenoid Ester 2	+ *	+ *	+ *	ns	- *	- *
Cis Lutein Ester	+ ***	+ ***	ns	ns	- **	- **
Lutein Ester 1	+ **	+ **	ns	ns	- *	- *

Table S3. Linear relationships between skin carotenoid concentrations and colorimetric variables. Related to Figure 2. Reproduced from Freeborn [S1]. Significance codes: 0 '***' 0.001 '**' 0.01 '*' not significant 'ns'. B: brightness, S_R: red, S_Y: yellow, S_G: green, S_B: blue, S_V: violet.

Population	Color	Pop	gene	Polymorphic gene	Fixed gene	corrected chi2	pvalue	qvalue	significant
Bastimentos West	All	BW	*ttc39b*	27	91	2.4085	0.0091	0.1207	FALSE
	Red	BW-R		25	91	1.5884	0.0414	0.2076	FALSE
	Yellow	BW-Y		19	96	3.8431	0.0016	0.0499	TRUE
Colon	Green	CL-G		17	96	4.8832	0.0003	0.0271	TRUE
Dolphin Bay	All	DB	*kit*	105	170	0.3854	0.2726	0.5347	FALSE
	Red	DB-R		76	171	0.5117	0.2506	0.4744	FALSE
	Blue	DB-B		60	172	2.8373	0.0050	0.0921	FALSE
Shark Hole	Blue	SK-B		54	174	5.9185	0.0001	0.0150	TRUE

Table S4. HKA test. Related to Figures 3 and 4. This test shows reduced polymorphism in genes of interest in non-red populations. Population abbreviations are the same used in Figure 1: DB (Dolphin Bay), SK (Shark Hole), CL (Colón), BW (Bastimentos West).

gene	morph 1	morph 2	Pairwise differences (pi)	Shared sites (k)	dT = pi /(2*mu*k)
ttc39b	BW- yellow	BW-red	27.8	7960	1,746,231
psip1	BW- yellow	BW-red	45.38	17136	1,324,113
kit	DB-blue	DB- red	16.39	11251	728,380
bco1	PO-green	TB-red	19.69	3734	2,636,583
	CL-green	DB-red	21.52	3740	2,877,005

Table S5. Haplotype divergence time. Related to Figures 3, 4 and 5. Average haplotype divergence time (years) between non-red color morphs and a red morph. Population abbreviations are the same used in Figure 1: DB (Dolphin Bay), PO (South Popa), CL (Colón), BW (Bastimentos West), and TB (Tranquilo Bay).

Organism	Amino acid substitution Protein Sequence	HS	NS	Conditions	ClinVar variant identifier
O. pumilio	**Val533Ile**	**4.20 > 4.50**	C>T		
Human	Ile542Met Ile542Phe	4.50 > 1.90 4.50 > 2.98	T>G A>T	Gastrointestinal stromal tumor; Hereditary cancer-predisposing syndrome	NM_000222.3(KIT):c.1626T>G (p.Ile542Met) NM_000222.3(KIT):c.1624A>T (p.Ile542Phe)
O. pumilio	**Gly959Arg**	**-0.40 > -4.50**	C>T		
Human	Asp974Glu Asp974Gly Asp974Asn	-3.50 > -3.50 -3.50 > -0.40 -3.50 >	C>G A>G G>A	Gastrointestinal stromal tumor	NM_000222.3(KIT):c.2922C>G (p.Asp974Glu) NM_000222.3(KIT):c.2921A>G (p.Asp974Gly) NM_000222.3(KIT):c.2920G>A (p.Asp974Asn)
O. pumilio	Glu960	-3.50			
Human	Asp975His Asp975Asn Asp975Gly Asp975Glu	-3.50 > -3.20 -3.50 > -3.20 -3.50 > -0.40 -3.50 > -3.50	G>C G>A A>G T>A	Mastocytosis Gastrointestinal stromal tumor **Piebaldism : refers to the absence of mature melanin-forming cells (melanocytes) in certain areas of the skin and hair** Hereditary cancer-predisposing syndrome	NM_000222.3(KIT):c.2923G>C (p.Asp975His) NM_000222.3(KIT):c.2923G>A (p.Asp975Asn) NM_000222.3(KIT):c.2924A>G (p.Asp975Gly) NM_000222.3(KIT):c.2925T>A (p.Asp975Glu)

Table S6. Synonymous and non-synonymous SNPs in Kit. Related to Figure 3. Each blue row names the position and amino acid substitution in kit for *O. pumilio*, and the following white rows correspond to mutations in the aligned position of the human kit ortholog. Substitutions are named following the convention (initial amino acid)-(position)-(final amino acid). Hydrophobicity (HS) of the initial and final amino acids are relative to the Kyte-Dolittle Hydrophobicity Scale. Nucleotide substitutions (NS) and associated conditions in humans are taken from the ClinVar database.

Supplemental Reference

S1. Freeborn, L.R. (2020). The Genetic, Cellular, and Evolutionary Basis of Skin Coloration in the Highly Polymorphic Poison Frog, Oophaga pumilio.